Experiments in Fluids (2024) 65:76
https://doi.org/10.1007/s00348-024-03817-w

RESEARCH ARTICLE

Friction Velocity Determination Techniques in Turbulent Boundary Layers with Miniature Vortex Generators

Jiahao Kong[1] · Bagus Nugroho[2] · Luke G. Bennetts[3] · C. I. Chan[4] · R. C. Chin[1]

Received: 25 January 2024 / Revised: 28 March 2024 / Accepted: 17 April 2024 / Published online: 7 May 2024

Abstract
Miniature vortex generators (MVGs) have the potential to control turbulent boundary layers (TBLs). Analyzing the scaled turbulent structure of MVG TBLs in experiments typically requires indirect methods for accurate friction velocity U_τ determination. The established methods for U_τ determination need to be verified for non-generic TBLs, such as MVG TBLs, especially at near-wake stations. This study compares the performance of the five most common U_τ-determination methods when applied to MVG TBLs. The methods are tuned in terms of their free parameters and fitting ranges using direct measurements of U_τ from large eddy simulation data, and applied to a corresponding experiment to assess their accuracy. Based on the findings, an "inner" method, which is the Musker function with a drifting buffer layer incorporating a bump function, is recommended for MVG TBLs of the form investigated, as it provides a good estimation of U_τ with uncertainty $< 3\%$ for all streamwise stations. The method is applied to three further experimental tests with different flow conditions to study trends in U_τ. The error of the drag variation is $< 6\%$, which indicates the method is reliable for MVG TBLs at high Reynolds numbers.

1 Introduction

Flow separation is encountered when a fluid moves against an adverse pressure gradient (increasing static pressure in flow direction), such as when air flows over aircraft wings/airfoils. The separation zone causes an increase in pressure drag, which incurs a large energy loss. Vortex generators (VGs) are used as a passive control to delay or prevent such flow separation, thus reducing the separation-induced pressure drag by introducing streamwise vortices to re-energize the near-wall separated flow (Lin 1999). VGs typically consist of pairs of triangular or rectangular blades mounted vertically on a wall and arranged in a spanwise array with respect to the incoming flow. Despite their advantages, VGs introduce a considerable pressure drag due to the fluid flow blockage created by the VGs. This behavior is known as device drag, which, in turn, reduces fuel efficiency in applications (Lin et al. 1989).

Conventional VGs are defined to have blade heights h on the order of the boundary layer thickness δ_0 ($h/\delta_0 \sim 1$). Low-profile VGs were introduced ($h/\delta_0 \leq 0.5$) to reduce device drag, while showing comparable effectiveness to conventional VGs because the small blades of low-profile VGs provide similar momentum transfer in the near-wall region compared to conventional VGs (Lin 2002). Low-profile VGs with a ratio $h/\delta_0 = 0.1$–0.2 are commonly referred to as miniature vortex generators (MVGs). Lin (1999) suggested that MVGs are most effective in a counter-rotating arrangement, where they can produce a substantial drag reduction up to 50% for laminar separated flows. Their ability to control separation has been investigated experimentally and numerically for low-speed and supersonic laminar flows (Lin et al. 1991; Lin 2002; Godard and Stanislas 2006; Panaras and Lu 2015), and they have been applied in engineering systems, including aircraft wings, compressor blades and wind tunnel blades (Lin 2002). MVGs are also used to delay laminar flows transitioning to turbulence (transitional boundary layer flows), thus reducing friction drag by shifting the transition point downstream (Fransson et al. 2006). Sattarzadeh et al.

✉ Jiahao Kong
jiahao.kong@adelaide.edu.au

[1] School of Electrical and Mechanical Engineering, University of Adelaide, Adelaide, South Australia 5005, Australia

[2] Department of Mechanical Engineering, University of Melbourne, Melbourne, Victoria 3010, Australia

[3] School of Computer and Mathematical Sciences, University of Adelaide, Adelaide, South Australia 5005, Australia

[4] Graduate School of Engineering Science, Osaka University, 1-3 Machikaneyama, Toyonaka, Osaka 560-8531, Japan

(2014) indicate that the net drag reduction could reach 65% when the transition delay is preserved by placing two arrays of MVGs at different streamwise locations.

MVG effects on turbulent flows are strong because MVGs impose large-scale vortical motions in turbulent boundary layers (TBLs), and, hence, MVGs are explored for TBL flow control. In particular, MVGs play a key role in interacting with the turbulent flows at near-wake stations (Ye et al. 2016; Lögdberg et al. 2009) and, thus, it is necessary to enhance the understanding of the MVG TBLs at near-wake stations to characterize the MVG effects. A large eddy simulation (LES) TBL study at moderate friction Reynolds numbers (up to $\mathrm{Re}_\tau \approx 1350$) reported that MVGs induce both large-scale counter-rotating primary vortex pairs and secondary vortical motion near the wall (Chan and Chin 2022). Lögdberg et al. (2009) conducted studies at a higher friction Reynolds number ($\mathrm{Re}_\tau \approx 3700$) that also indicate the development of MVG-induced streamwise vortices in the near-wall region. However, they did not analyze MVG effects based on the scaling of friction velocity due to the challenge of determining U_τ for MVG TBL experiments. Farther from the wall, the TBL is a non-equilibrium flow that experiences a spanwise variation in the log region and the outer layer (Ye et al. 2016). Many well-known U_τ-determination methods (such as Clauser method Clauser 1954), developed for canonical TBLs (i.e., smooth-wall-bounded flow), depend on the log-law of the wall. Under the influence of MVGs, the log region is heavily altered (Ye et al. 2016). Because of this situation, determining skin friction velocity using standard techniques may not be suitable for MVG TBLs and need to be assessed.

Direct measurements are another approach to determine U_τ in experiments. They involve a floating element to measure the drag force directly (Krogstad and Efros 2010; Baars et al. 2016). However, this is challenging for MVG TBLs because the drag-balance devices have experimental limitations on measuring friction velocity at different streamwise locations (space limitation) (Hakkinen 2004). It would be prohibitively expensive to have a drag balance that covers an entire wind tunnel test section or to arrange it to be movable in the downstream direction. The friction velocity can also be determined using the momentum integral equation based on the streamwise derivative of the momentum thickness. This method also has its challenges, requiring sensor systems that can move downstream, i.e., a hot-wire or pitot tube that is attached to the rail. Further, this method has been reported to overestimate U_τ for flows experiencing secondary motions (Lögdberg et al. 2009; Nugroho et al. 2013).

Generally, the skin friction velocity can be determined indirectly with the concept of wall similarity, which itself can be classified into three categories: outer-layer similarity, linear log-law and inner-layer similarity. The first category, based on the outer-layer similarity, involves the velocity defect profile, which relies on the existence of the universal defect law to determine U_τ (Monty et al. 2011; Kong et al. 2023). Such universal velocity defects are observed in the wake region from 0.4δ for MVG TBLs, where δ is the boundary layer thickness (see Figure 7 of Chan and Chin (2022)). The second category is the linear log-law, in which the modified Clauser chart (MCC) and log-law slope (LLS) methods utilize such a law to estimate U_τ (Schultz and Swain 1999; Flack et al. 2007). Both methods are used to estimate U_τ for non-generic TBLs, for example, rough-wall TBLs (Squire et al. 2016), TBLs over riblets surfaces (Nugroho et al. 2013; Cui et al. 2019; Xu et al. 2019) and cavities (Scarano et al. 2022). The LLS method is also used to estimate U_τ experimentally for the MVG TBL by Ye et al. (2016) at downstream stations where the streamwise velocity profiles show a log layer. The third category is the inner-layer similarity technique, where the method uses the Musker function (Musker 1979; Chauhan et al. 2009). Apart from being used to determine U_τ for smooth-wall TBLs (Rodríguez-López et al. 2015), the Musker function is also used to estimate U_τ for the non-generic TBLs, including TBLs transitioning from a rough surface to a smooth wall (Li et al. 2019), modified by spanwise periodic trips (Rodríguez-López et al. 2016; Buxton et al. 2018) and when the flow interacted with synthetic jets (Ye et al. 2019). Since the velocity profiles of MVG TBLs show collapsing viscous sublayers and shifted log layers at near-wake stations (Chan and Chin 2022), the Musker function can be adapted and further developed to determine U_τ for MVG TBLs from near-wake stations.

The U_τ-determination approaches mentioned above have been applied to non-generic TBL experiments, but only at downstream stations because the approaches rely on the assumption that the inner layer redevelops and behaves as the smooth-wall TBL (Rodríguez-López et al. 2016; Ye et al. 2016). The suitability and accuracy of the indirect methods in determining U_τ for MVG TBLs at near-wake stations experiencing an inner-layer modification are unknown. Without accurate friction velocity information, the understanding of MVG effects on the mean statistics and flow structures remains limited for high Reynolds number MVG TBL flows (Lögdberg et al. 2009). Hence, there is a need to assess and improve the U_τ-determination methods for MVG TBL flows experiencing an inner-layer modification.

The present study investigates the above-mentioned U_τ-determination techniques by adapting the procedures and the fitting ranges of the techniques for MVG TBLs from the near-wake station. The five techniques are reviewed in Sect. 2. The LES MVG data of Chan and Chin (2022) is used to verify the U_τ-determination techniques in Sects. 4.2, 4.3 and 4.4. Then, the techniques are applied to new experimental data (summarized in Sect. 3) in Sect. 4.5.

2 Description of friction velocity determination methods

The classic "two-layer" model for TBL mean velocity profiles contains an inner layer U^+_{inner}, an outer layer U^+_{outer} and a logarithmic layer in the overlap region between the inner and outer layers. The superscript + indicates the scaling of viscous units, namely the friction velocity U_τ and the viscous length $l_\nu = \nu/U_\tau$, for instance, $y^+ = yU_\tau/\nu$. The friction velocity is estimated using three wall-similarity methods based on the above three feature layers: the inner-layer, log-law and outer-layer methods.

2.1 Outer-layer similarity methods

The defect profile method utilizes the outer-layer similarity hypothesis to determine U_τ. This hypothesis states that the outer layer is unaffected by the wall condition at a sufficiently large Reynolds number (Townsend 1974) and follows a universal defect law as the velocity defect wake function (Hama 1954), such that

$$\frac{U_\infty - U}{U_\tau} = -\frac{1}{\kappa}\ln\left(\frac{y}{\delta}\right) + \frac{\Pi}{\kappa}\left[w(1) - w(\frac{y}{\delta})\right], \tag{1}$$

where U_∞ is free-stream velocity, κ is the von Kármán constant, w is the wake function and $\Pi = 0.45$ is the wake constant (Nagib and Chauhan 2008). Djenidi et al. (2019) suggested a universal defect profile as the reference for rough-wall TBLs in the form $(U_\infty - U)/U_\tau = f(y/\delta)$. The method is as follows: (i) The reference defect profile is obtained from a smooth-wall TBL and scaled by U_τ; (ii) the measured data $U_\infty - U$ (i.e., rough-wall flows have the outer layer from $y = 0.15\delta$ (Djenidi et al. 2018), MVG TBL flows) is fitted onto the reference profile by adjusting U_τ; and (iii) U_τ is determined when the fitting result reaches the least square error. The advantages of the defect profile method are summarized by Djenidi et al. (2019) and Monty et al. (2011).

2.2 Log-law methods

The Clauser chart method, proposed by Clauser (1954), was the first to utilize the log layer to determine U_τ for smooth-wall TBLs as

$$\frac{U}{U_\tau} = \frac{1}{\kappa}\ln\left(\frac{yU_\tau}{\nu}\right) + C, \tag{2}$$

where $C = 5.3$ is an additive constant for the smooth-wall TBL and ν is the kinematic viscosity. An adapted form of the Clauser chart method proposed by Lewthwaite et al. (1984), named the log-law slope method (Walker 2014) (LLS) can be used to determine U_τ for TBLs with the shifting log-law layer. The log-law equation (Eq. 2) can be rewritten by substituting $U_\tau = U_\infty\sqrt{c_f/2}$ as follows

$$\frac{U}{U_\infty} = \frac{\sqrt{c_f/2}}{\kappa}\ln\left(\frac{yU_\infty}{\nu}\right) + \frac{\sqrt{c_f/2}}{\kappa}\ln\left(\sqrt{\frac{c_f}{2}}\right) + \sqrt{\frac{c_f}{2}}C, \tag{3}$$

where $c_f = 2U_\tau^2/U_\infty^2$ is the local skin friction coefficient. When all measured points are plotted in the form of U/U_∞ versus yU_∞/ν, the slope of the log region $\sqrt{c_f/2}/\kappa$ can be found by the least square error analysis. Hence, the friction velocity U_τ can be estimated from c_f. Note that this method requires defining the log-law region properly, and any points in the viscous sublayer must be excluded to employ this method successfully (Walker 2014). The fitting range for smooth- and rough-wall TBLs is suggested as $y^+ = 2.5\sqrt{\text{Re}_\tau}$ to $y = 0.15\delta$ (Walker 2014).

The present study investigates a second method utilizing the linear log-law to determine U_τ for TBLs with the shifting log-law layer, which is commonly known as the modified Clauser chart method that was used by Perry and Li (1990). The equation for the modified Clauser method is derived from the velocity defect law in the log-law layer part (Perry and Li 1990) (see Eq. 1). The equation of the defect law is

$$\frac{U_\infty - U}{U_\tau} = -\frac{1}{\kappa}\ln\left(\frac{y}{\delta}\right) + \frac{2\Pi}{\kappa}. \tag{4}$$

By substituting $\delta = \kappa U_\infty \delta^*/(1+\Pi)U_\tau$ (Coles 1956), Eq. 4 can be rewritten as

$$\frac{U}{U_\infty} = 1 + \frac{1}{\kappa}\frac{U_\tau}{U_\infty}\ln\left(\frac{y}{\delta^*}\right) + \frac{1}{\kappa}\frac{U_\tau}{U_\infty}\left(\ln\left(\frac{U_\tau}{U_\infty}\right) + \ln\left(\frac{1+\Pi}{\kappa}\right)\right) - \frac{U_\tau}{U_\infty}\frac{2\Pi}{\kappa}, \tag{5}$$

where δ^* is the displacement thickness. Measured data are plotted as U/U_∞ versus $\ln(y/\delta^*)$. The data points in the fitting range $y/\delta^* = 0.25$–0.9 were compared with a family of linear constant lines with slopes of $U_\tau/\kappa U_\infty$. The friction velocity is obtained when the fitting between constant lines and the log-law data points reaches the least square error. Perry and Li (1990) found that this method can estimate U_τ within ±3% error. Hence, the present study will apply those two methods utilizing the log-law and examine the existence of the log-law in MVG TBL profiles.

2.3 Inner-layer similarity methods

As MVG TBLs develop over a smooth wall, the anisotropy state in the near-wall region remains unchanged for MVG-influenced flows, which indicates that the near-wall flow dynamics are similar to the smooth-wall TBL (Angele and

Muhammad-Klingmann 2016). The near-wall layer contains the viscous sublayer, the log-law layer and the buffer layer (adapting the previous two layers). There are three functions used to describe the inner-layer profile, which are introduced by Spalding, Van Driest and Musker (found in Chauhan et al. (2007)). As the forms of Spalding and Van Driest are not straightforward to fit the velocity profile of U versus y, the present study chooses the Musker function in the inner-layer similarity method.

Musker (1979) developed an adaption function of the buffer layer to asymptotically connect the viscous sublayer and the linear log-law layer. The Musker function is given as

$$U^+_{\text{inner}}(\text{Musker}) = \frac{1}{\kappa}\ln\left(\frac{y^+_* - a}{-a}\right) + \frac{P^2}{a(4\alpha - a)} \left[(4\alpha + a)\ln\left(-\frac{a}{P}\frac{\sqrt{(y^+_* - \alpha)^2 + \beta^2}}{y^+_* - a}\right) + \frac{\alpha}{\beta}(4\alpha + 5a)\left(\arctan(\frac{y^+_* - \alpha}{\beta}) + \arctan(\frac{\alpha}{\beta})\right)\right], \tag{6}$$

where $\alpha = (-1/\kappa - a)/2$, $\beta = \sqrt{-2a\alpha + \alpha^2}$ and $P = \sqrt{\alpha^2 + \beta^2}$. $y_* = y + \epsilon$, where ϵ is the wall-normal distance offset. The key feature of this function is that the parameters a and κ can be adjusted to output various additive constant C in Eq. 2. For the MVG TBLs, Chan and Chin (2022) reported that the additive constant C spans a range, $C = 3.2$–5.2 from the near-wake stations, where the inner layers show a collapsing viscous sublayer, but various buffer layers. The procedure for the MVG TBL needs to be adjusted by relaxing the constant a to generate various inner-layer profiles with a range of additive constant C. The procedure detail is illustrated in the following optimization technique. Then, the Musker function may provide an appropriate description for the inner-layer profiles of MVG TBLs. Note that there is a flaw in the Musker function for smooth-wall TBLs reported by Chauhan et al. (2007) and Rodríguez-López et al. (2015). This function cannot reflect an overshoot near $y^+ \approx 50$ in the buffer region. Monkewitz et al. (2007) developed a "hump" function to modify the Musker function, and this modified function shows better agreement with the smooth-wall experimental data in the buffer layer (Chauhan et al. 2007; Rodríguez-López et al. 2015). The modified Musker function is

$$U^+_{\text{inner}}(\text{modified}) = U^+_{\text{inner}}(\text{Musker}) + \frac{\exp\left[-\ln^2(y^+_*/30)\right]}{2.85}. \tag{7}$$

In the present study, the two inner-layer methods, adopting a modified procedure to generate various inner-layer profiles with the Musker function U^+_{inner}(Musker) and modified Musker function U^+_{inner}(modified), are referred to as "inner1" and "inner2," respectively.

Both inner-layer functions depend on U_τ, a, ϵ, and κ. For the optimization process, this study employs a technique similar to that of Rodríguez-López et al. (2015), which determines the friction velocity for the smooth-wall TBL with the composite profile method. As suggested by the reference technique, the target function for this technique can be defined as follows

$$E(U_\tau, a, \epsilon, \kappa) = \frac{|U^+_{\text{inner}}(U_\tau, a, \epsilon, \kappa) - U^+_{\text{measured}}(U_\tau)|}{U^+_{inner}(U_\tau, a, \epsilon, \kappa)}, \tag{8}$$

where U^+_{inner} is the reference inner-layer function and U^+_{measured} is the target profile from the experimental measurement. Rodríguez-López et al. (2015) suggested this error function provides accurate U_τ determination because the function gives greater weighting to the data close to the wall.

The optimization problem can be described as

$$\text{find min}[E(U_\tau,\ a)],\quad \text{subject to}\begin{cases} U_\tau \in [U_{\tau,min}, U_{\tau,max}], \\ a \in [a_{min},\ a_{max}], \\ \epsilon \in [\epsilon_{min},\ \epsilon_{max}], \\ \kappa \in [\kappa_{min},\ \kappa_{max}]. \end{cases} \tag{9}$$

The bounds of four variables are set to increase the robustness of this technique (Rodríguez-López et al. 2015). The bounds are selected to be far enough from the optimal results after each optimization to ensure the optimization process is not affected by the bounds. The ranges for U_τ and a are $U_\tau = 0.5U_{\tau,i}$–$1.5U_{\tau,i}$ and $a = 0.5a_i$–$1.5a_i$. The initial conditions have been selected as typical and reasonable values for two variables. The initial $U_{\tau,i}$ is determined by the defect profile method and the initial a_i is -10.58, which yields $\kappa = 0.41$ and $C = 5.2$ for smooth-wall TBLs (Rodríguez-López et al. 2015). The bounds of ϵ are set to cover the uncertainty of the wall distance. The bounds of κ are 0.3–0.5, which covers the known range of $\kappa = 0.384$–0.42 (Nagib and Chauhan 2008). The initial values for two variables are $\epsilon = 0$ and $\kappa = 0.41$.

The optimization problem is defined in terms of the Lagrangian problem $\mathcal{L}(\boldsymbol{x_k}, \lambda) = E(\boldsymbol{x_k}) - \lambda^T \boldsymbol{b}(\boldsymbol{x_k})$, where E is the residual error function of Eq. 8, $\boldsymbol{x_k}$ is the optimized variables, $\boldsymbol{b}$ is the constraining bounds of two variables and λ is the Lagrange multiplicators. The optimization problem is solved using sequential quadratic programming (Nocedal and Wright 2006). The Lagrangian problem $\mathcal{L}$ is approached by a quadratic subproblem. For an iterate $\boldsymbol{x_k}$, an appropriate search direction $\boldsymbol{d_k}$ can be found as a solution to the quadratic subproblem

$$\text{find } \min_{d}\left[E(\boldsymbol{x_k}) + \nabla E(\boldsymbol{x_k})^T\boldsymbol{d} + \frac{1}{2}\boldsymbol{d}^T\nabla^2 E(\boldsymbol{x_k})\boldsymbol{d}\right], \quad \text{subject to } \boldsymbol{b}(\boldsymbol{x_k}) + \nabla\boldsymbol{b}(\boldsymbol{x_k})^T\boldsymbol{d} \geq 0. \tag{10}$$

Once the solution of the quadratic subproblem is determined, the next iterate step is $\boldsymbol{x_{k+1}} = \boldsymbol{x_k} + \boldsymbol{a_k}\boldsymbol{d_k}$, where $\boldsymbol{a_k}$ is the step length parameter. The sequential quadratic programming is implemented with a MATLAB function *fmincon*. As suggested by Rodríguez-López et al. (2015), the tolerances of variables $\boldsymbol{x_k}$ and the error function E are set to 10^{-10}.

The inner1 and inner2 methods utilize the measured data from the wall to the log layer as per the definition of two inner-layer functions. The outer bound is selected as $y_O^+ = 3\sqrt{\mathrm{Re}_\tau}$, which is considered as the onset of the log region (Marusic et al. 2013; Monkewitz et al. 2007; Nagib et al. 2007). Hence, the data from the wall to $y^+ = 3\sqrt{\mathrm{Re}_\tau}$ will be used for the two inner-layer methods.

3 Experimental setup and database details

3.1 Facility

The experiment of the flat plate TBL measurements are conducted at the closed-loop wind tunnel at the University of Adelaide. The maximum speed of the wind tunnel is $30\,\mathrm{m\,s^{-1}}$. The airflow goes through three layers of meshes and one layer of honeycomb grid, then comes out from a square cross-sectional outlet of $0.5 \times 0.5\mathrm{m}^2$, which can maintain a low turbulence level of approximately 0.5%. The wind tunnel is attached with a working section of length 2 m and a rectangular cross-sectional area of $0.5 \times 0.3\mathrm{m}^2$. A 1.9 m long aluminum plate is mounted on the bottom surface of the test section. The sidewalls are adjustable to compensate for the boundary layer growth to maintain zero pressure gradient (ZPG; i.e., constant static pressure in flow direction). A tripping device of a 36 grit sandpaper of length 100 mm is mounted at the leading edge to ensure flows develop to TBLs.

3.2 MVG configuration

The experimental measurements utilize a rectangular vane-type MVG placed in a "V" shape. The MVG configuration and geometry are shown in Fig. 1 and summarized in Table 1. The coordinate system is chosen with the origin at the leading edge centerline of the aluminum flat plate. The Cartesian coordinates x, y and z correspond to the streamwise, wall-normal and spanwise directions, respectively, with corresponding velocity components U, V and W. The symbols $\bar{(\cdot)}$ and $(\cdot')$ denote the temporal-averaged and fluctuation of velocity signals, respectively. The point x^* is the streamwise distance downstream of the MVG array, $x^* = x - x_M$, where x_M is the location of the MVG array. The boundary layer thickness δ is defined at which the velocity reaches $U/U_\infty = 0.99$. δ_0 is the boundary layer thickness at MVG location $x = x_M$.

The metal MVG vanes are affixed on the aluminum flat plate with a height of $h = 3$ mm, a thickness of $w = 0.75$ mm and a length of $L = 7.5$ mm. The angle of attack (AOA) of the MVG with respect to the flow direction is 15°. The

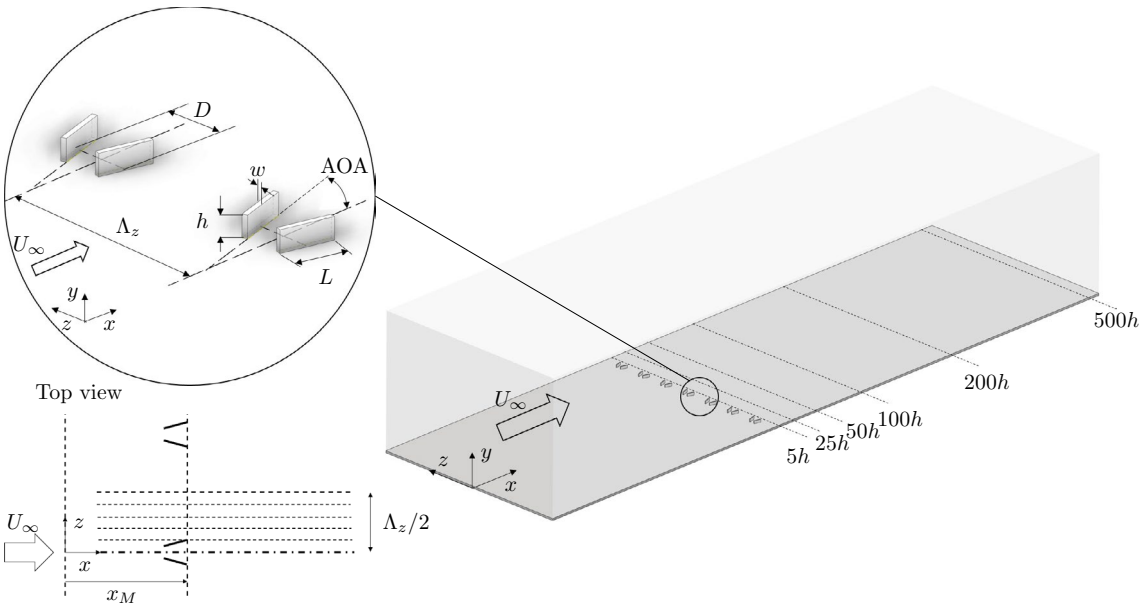

Fig. 1 Schematic views of flow domains and MVG configuration. x_M is the MVG location defined from the trailing edges of the tripping device

Table 1 All MVG configurations for experimental and LES MVG database (Chan and Chin 2022). The LES MVG database's dimensional parameters are scaled with the inlet displacement thickness, δ_0^*. Most geometry ratios of MVGs are identical except for h/δ_0. The color of × denotes the color code of six streamwise locations

Case	Flow conditions			MVG geometries							x^* position					
	U_∞(m s^{-1})	$Re_{\tau 0}$	x_M(m)	h/δ_0	h(mm)	AOA	Λ_z/h	L/h	D/h	w/h	5 h	25 h	50 h	100 h	200 h	500 h
EXP1	7.4	400	0.41	0.18	3	15°	10	2.5	2.5	0.25	×	×	×	×	×	×
EXP2	20	900	0.41	0.18	⋯						×	×	×	×	×	×
EXP3	7.4	650	1.31	0.1	⋯						×	×	×	×	×	
EXP4	20	1500	1.31	0.1	⋯						×	×	×	×	×	
LES MVG	U_∞	$Re_{\tau 0}$	x_M	h/δ_0	h	AOA	Λ_z/h	L/h	D/h	w/h	5 h	25 h	50 h	100 h	200 h	500 h
	1	430	950	0.19	–	15°	10	2.5	2.5	0.25	×	×	×		×	×

geometry ratios for the spanwise distance between the centroids of MVG vanes in one pair and the spanwise distance between MVG pairs are $D/h = 2.5$ and $\Lambda_z/h = 10$, respectively. A total of thirteen pairs of MVGs span a width of 420 mm, covering the entire width of the test section. The geometrical ratios are identical to those of the LES study by Chan and Chin (2022).

MVG TBLs with different ratios of h/δ_0 and friction Reynolds numbers Re_τ were performed. The variation of h/δ_0 is implemented by mounting the MVG array at two locations, $x_M = 0.41$ m and $x_M = 1.31$ m. As boundary layer thickness becomes larger for the downstream location, the ratio of h/δ_0 varies from 0.18 to 0.1, where the higher one is similar to those used by Lögdberg et al. (2009) and Chan and Chin (2022). For MVG configuration of each ratio of h/δ_0, MVG TBLs are performed at two free-stream velocities $U_\infty = 7.4$ and 20 m s^{-1}. Hence, the present study has four experimental sets as per Table 1. The reference result is provided from the LES MVG database of Chan and Chin (2022) in Table 1. The LES is performed using a fully spectral numerical code (Chevalier et al. 2007). The computational domain uses $6144 \times 513 \times 768$ nodes in the streamwise, wall-normal and spanwise directions, respectively. The LES MVG TBL was sampled by a total of 429 spanwise profiles at each streamwise station of $x^*/h = 5$, 25, 50, 200 and 500. The time statistics are sampled for a minimum duration $T = 7\delta/U_\tau$, and the quality of statistics was validated by Chan and Chin (2022).

3.3 How many spanwise velocity profiles are enough to obtain spanwise-averaged profiles?

One of the main challenges in characterizing wall-bounded flows experiencing high and low momentum in the wall-normal direction over a spanwise distance is the variations of U_τ and ΔU^+. Chan and Chin (2022), Lögdberg et al. (2009), Shahinfar et al. (2014), Koeltzsch et al. (2002), Nugroho et al. (2013) and Kevin et al. (2017) show that low-profile vortex generators, such as MVGs and directional riblets, can generate large-scale vortices that vary the streamwise mean velocity and turbulence intensity over a spanwise area. Such variations eventually modify the U_τ- and ΔU^+-values spanwisely. One method to properly characterize the spanwise-varied flows is via spanwise averaging the turbulence statistics over a certain spanwise distance, i.e., over half wavelength of the vortex generator. Such a method was applied to the directional riblets study successfully by Nugroho et al. (2013).

This study determines the friction velocity using the spanwise- and temporal-averaged velocity profiles at various streamwise locations. Spanwise- and temporal-averaged profiles of the mean velocity and turbulence intensity are referred to as "global profiles" as those results reflect the global effect of the spanwise variation on the streamwise mean velocity and turbulence intensity. Spanwise and wall-normal flow field measurements of the global profiles were obtained downstream of the MVG array. However, before such an assessment is conducted, it is necessary to determine how many individual spanwise profiles are sufficient to determine the global profiles accurately. We utilize the LES MVG data of Chan and Chin (2022) to investigate the sufficient number of individual spanwise profiles.

Taking advantage of the high spatial resolution of the LES MVG database, true-global velocity profiles were obtained by averaging 429 spanwise velocity profiles over a spanwise length of $-2.5\Lambda_z \le z \le 2.5\Lambda_z$ from the LES MVG database (referred to as "true-global profile"). The "true" U_τ is referred to the mean U_τ value from 429 individual profiles for the LES MVG database, i.e., the true U_τ is computed by averaging 429 U_τ-values from individual spanwise profiles. Pseudo-global profiles were also computed by averaging various numbers of linearly spaced individual profiles between 2 to 44 from the LES study over half spanwise wavelength of one side of MVG, $0 \le z \le \Lambda_z/2$. The pseudo profiles are compared with the true-global profiles at $x^*/h = 5$–500 using the mean relative error defined as

$$\epsilon_y|_{\text{pse}}(\%) = 100 \times \left\langle \frac{|U_{\text{pse}} - U_{\text{true}}|}{U_{\text{true}}} \right\rangle_y, \tag{11}$$

where U_{pse} and U_{true} are the pseudo and true-global velocity profiles, respectively. The notations ϵ_y and $\langle\cdot\rangle_y$ denote a wall-normal averaged error and the wall-normal averaging, respectively. The wall-normal averaging is computed with 100 logarithmically spaced points for a region of $y/\delta = 0.01$–1, which will give a greater weighting to the points close to the wall where the velocity is smaller. The mean relative error is plotted against the linearly spaced profile numbers in Fig. 2a. The mean relative error reduces with the increase of linearly spaced profiles number. The error is $\epsilon_y|_{\text{pse}} < 0.2\%$ when ≥ 6 profiles are used. This outcome indicates that six linear-spaced spanwise profiles can determine the global profile accurately with a low uncertainty level of $\approx 0.2\%$ for streamwise locations of $x^*/h = 5$–500. More spanwise profiles can only provide limited improvement in the accuracy of the global profile determination.

Figure 2b compares the true and pseudo global profiles. The dash-line profiles are the pseudo profiles computed by averaging six individual spanwise profiles over half spanwise wavelength, $0 \leq z \leq \Lambda_z/2$. The solid-line profiles are the true-global profiles by spanwise averaging a total of 429 profiles over a spanwise length of $-2.5\Lambda_z \leq z \leq 2.5\Lambda_z$. For $x^*/h = 5$–500, all pseudo profiles (dash line) collapse well with the true profiles (solid line). This outcome indicates that the global profiles computed by averaging six profiles are acceptable for streamwise development of $x^*/h = 5$–500.

3.4 Velocity measurement

The MVG TBL velocity measurements were taken by using hot-wire anemometry (HWA). The HWA is an in-house designed constant temperature anemometer following the design of Perry (1982). All results were obtained using single-wire boundary-type probes soldered with Platinum-Wollaston wires as sensor filaments. The diameter and length of sensor filaments are $d = 2.5\,\mu$m and $l = 0.5$ mm, which gives the length-to-diameter ratio $l/d \geq 200$ to minimize attenuation due to end conduction effects (Ligrani and Bradshaw 1987; Hutchins et al. 2009). The HWA overheat ratio was set to $R_w/R_a = 1.8$, where R_a is the cold resistance of the sensor, and R_w is the operating resistance. The HWA system signal was sampled using a National Instrument Data Acquisition board (NI9234) with frequency $f_s = 51,200$ Hz. The sampling duration is set to $T = 120$ s, which can achieve the boundary layer turnover times $TU_\infty/\delta > 28000$ to make sure that all statistics are sufficiently converged (Hutchins et al. 2009).

The HWA signal was calibrated with an in situ Pitot tube for each 5 h measurement. A pitot tube was placed above the hot-wire probe, approximately 10 mm into the free-stream flow to determine the free-stream velocity with an electronic barometer (220DD Baratron, MKS). The flow temperature was monitored by a calibrated RTD-type thermocouple (Pt1000). The calibration profile is determined by fitting a fourth-order polynomial curve onto the pressure and hot-wire voltage signals. The intermediate calibration profile is obtained between pre- and post-calibration profiles to correct the temperature drift (Talluru et al. 2014). After each spanwise velocity profile measurement, the free-stream velocity measured by the Pitot tube was recorded and compared with the hot-wire signals in the free-stream flow. The whole dataset was discarded if the U_∞ difference between the Pitot tube and HWA signals was larger than 1%.

3.5 Traverse system

The wall-normal and spanwise flow field measurements (yz-plane) were measured at six streamwise locations, $x^*/h = 5$, 25, 50, 100, 200 and 500, as summarized in Table 1. Note that the cases of EXP3 and EXP4, where the MVGs were placed farther downstream at $x_M = 1.31$ m, cannot obtain the flow field at $x^*/h = 500$ due to the length limitation of the test section. For each yz-plane, six spanwise linear-spaced velocity profiles are obtained within $0 \leq z \leq \Lambda_z/2$. The wall-normal velocity profiles are taken from the near-wall location to the free-stream flow with varying measurement

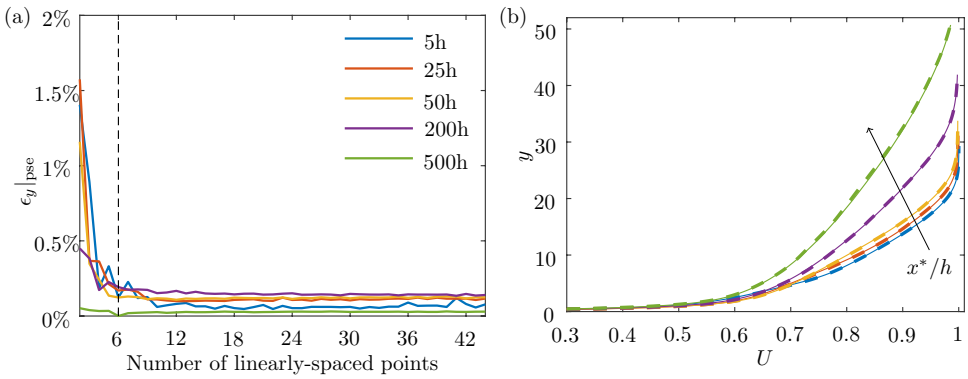

Fig. 2 Mean relative error versus the distance of interval (**a**); Comparison between the true-global velocity profiles (solid line) and pseudo global velocity profiles averaged over a half spanwise wavelength of one side of MVG, $0 \leq z \leq \Lambda_z/2$ with an interval, $0.1\Lambda_z$ (dash line) (**b**); Here, all data is from the LES MVG case. Color code refers to the symbol of × in Table 1

points of 30–50. The measurement grid points for each yz-plane were determined by multiplying the minimum spanwise profile number of 6 with the wall-normal points for each spanwise profile spanning a range of 30–50. Hence, the total grid points vary from 180–300 (6×30–6×50) at different streamwise locations. The traversing and collection of data processes were automatic and took approximately 10–20 h for each yz-plane. A 2D traverse system comprises horizontal and vertical sliding platforms equipped with two optical linear encoders and driven by micro stepper motors, which can perform horizontal and vertical traverses of the hot-wire probe with an accuracy of 5 μm and 0.5 μm, respectively.

The wall distance of the hot-wire probe for each velocity profile measurement was determined by using a digital microscope. A cylinder with a length of 18.79 mm was placed under the hot-wire probe. The hot-wire probe was moved to be close to the cylinder; then an image including the cylinder and hot-wire probe was photographed using a horizontally placed digital microscope. The distance between the sensor filament and the top of the cylinder was measured in the photograph so that the wall distance can be determined. Note that the accuracy of the wall distance given by this method depends on the pixel size of the microscope, which can achieve an accuracy of 0.008 mm. As the wall distance accuracy may influence the accuracy of U_τ-determination techniques, the sensitivity of the U_τ -determination techniques to such wall distance accuracy is analyzed in Sect. 4.5.

4 Result and discussion

4.1 Comparison between experimental and LES MVG databases

The boundary layer conditions for the LES MVG database (Chan and Chin 2022) at streamwise locations $x^*/h = 5,\ 25,\ 50,\ 200$, and 500 are summarized in Table 2. The mean velocity profiles, normalized by the outer-scaled length and velocity, δ and U_∞, respectively, are plotted in Fig. 3a. The profiles show a velocity deficit around the tip of MVGs at $y/\delta \approx 0.2$ for $x^*/h = 5$. The arrow indicates that the deficit decays with the downstream development and is eliminated at $x^*/h = 200$.

The corresponding mean velocity profiles of EXP1 are plotted in Fig. 3b. The velocity deficit of EXP1 reduces along the streamwise development for $x^*/h = 5$–50, which shows similar behavior to the LES MVG result. In addition, both results of LES and EXP1 cases collapse for $x^*/h \geq 200$, which indicates the velocity deficit becomes negligible after $x^*/h = 200$. Overall, the similar reduction behavior of the velocity deficit at $x^*/h = 5$–50 for the LES and the experimental result indicates that the experimental data and the global velocity profile determined by averaging six individual profiles is acceptable.

4.2 Applications of friction velocity determination methods to LES MVG database

The five friction velocity methods are applied to the LES MVG database with some assumptions to examine the efficacy at a preliminary stage in Sects. 4.2 and 4.3. For the inner-layer methods, two optimization variables are fixed for simplicity. The von Kármán constant is fixed at $\kappa = 0.41$, as suggested by the LES MVG database (Chan and Chin 2022), and the wall-normal offset is fixed at $\epsilon = 0$. In addition, the log-law methods (LLS and MCC) are based on the assumption of $\kappa = 0.41$ to maintain consistency among the five methods. The two inner methods are further verified for the LES MVG database with floating κ and ϵ in Sect. 4.4.

In order to investigate the efficacy of the five U_τ-determination techniques that are discussed in Sect. 2, the five methods are applied to the true-global mean velocity profiles from the LES MVG database by averaging a total of 429 spanwise velocity profiles at each yz-plane to estimate U_τ. The applications of the five methods are based on the typical fitting ranges for the smooth- and rough-wall data, as discussed in Sect. 2. The performance of the five methods is examined by analyzing an error between the estimated and true U_τ values (from the full LES MVG database) at five streamwise locations, which are computed as $E_{U_\tau}(\%) = 100 \times (U_\tau|_{\text{esti}} - U_\tau|_{\text{true}})/U_\tau|_{\text{true}}$, and summarized in Table 3. Note that we do not apply

Table 2 Boundary condition detail of the LES MVG database (Chan and Chin 2022)

x^*/h	δ	θ	δ^*	H	U_τ	$1000c_f$	Re_τ
5	21.86	2.77	4.18	1.51	0.0458	4.23	451
25	23.21	2.95	4.34	1.47	0.0444	3.93	468
50	24.80	3.15	4.60	1.46	0.0437	3.80	496
200	34.39	4.24	6.03	1.42	0.0423	3.58	660
500	52.28	4.31	6.12	1.42	0.0403	3.25	948

The thickness parameters are scaled with δ_0^*

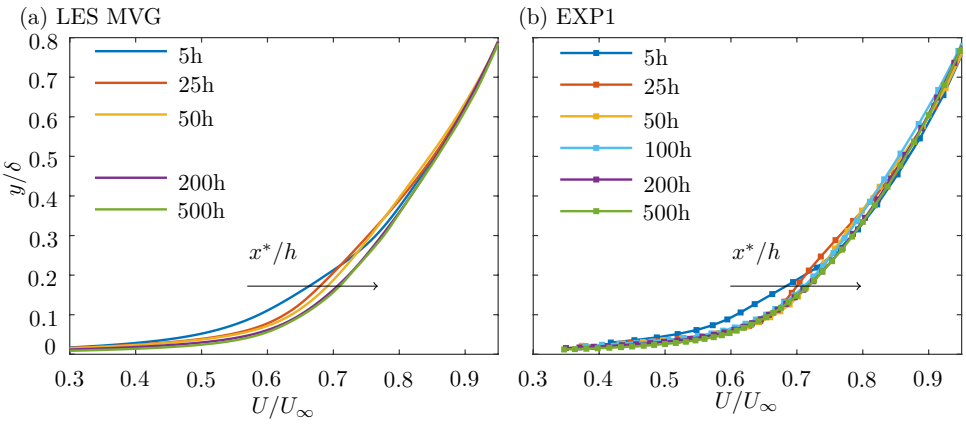

Fig. 3 Mean velocity profiles U/U_∞ versus y/δ for LES MVG database (**a**) and EXP1 (**b**); Color code refers to the symbol of × in Table 1. The data of LES MVG at 100h is not available

the defect profile method to the LES MVG database at $x^*/h = 500$ because the flow reaches its equilibrium and behaves similarly to the smooth wall, which already shows the validity of the defect profile method (Chan and Chin 2022). The performance of the five U_τ-determination techniques in Table 3 is analyzed in Sects. 4.2.1, 4.2.2 and 4.2.3.

4.2.1 Defect profile method

In Table 3, the defect method result shows the U_τ difference can be maintained below 1% at $x^*/h = 5$ and 200, but are greater than 3.8% at $x^*/h = 25$ and 50. The performance of the defect profile method varies with different fitting ranges. Here, the fitting ranges span over combinations of $0.1 \le y_I/\delta \le 0.6$ and $0.8 \le y_O/\delta \le 1.2$. Such combinations can cover the region of $y/\delta = 0.4$–1 showing outer-layer similarity for the LES MVG database.

The estimated U_τ result from the defect profile method is compared with the true U_τ of the LES MVG case and plotted in the form of a contour map of E_{U_τ} as shown in Fig. 4. The result shows that the estimation of the defect profile method is insensitive to the outer bound. The red circle indicates a minimum error of $E_{U_\tau} \approx 0.5\%$ for each streamwise location. The fitting range of the minimum error correlates with the inner bound, which moves away from the wall $y_I/\delta = 0.1$–0.6 with the downstream development from $x^*/h = 5$ to 50. Due to the different velocity deficits induced by MVGs, the outer-layer similarity layer is applicable for specific streamwise locations.

A universal fitting range can be selected based on the smallest fitting range generating the minimum error in Fig. 4, which is $y/\delta = 0.6$–1. The defect profile method is applied to the LES MVG database again to determine the U_τ values with this universal fitting range. The estimated U_τ values are 0.0434, 0.0431, 0.0439 and 0.0431 at $x^*/h = 5$, 25, 50 and 200, respectively, and the corresponding E_{U_τ} values are −5.6%, −2.7%, 0.7% and 1.9%. The estimated U_τ remains nearly constant and does not show dependence on the streamwise location, contrary to the true U_τ values (the LES MVG case in Table 3) showing U_τ monotonously decreasing along the downstream development. Hence, a universal fitting range of $y/\delta = 0.6$–1 for the defect profile method to determine U_τ is insufficient to reflect the actual behavior of U_τ induced by MVGs.

4.2.2 Log-law methods

Table 3 shows that the two log-law methods (LLS and MCC) cannot accurately estimate U_τ with $E_{U_\tau} \approx 20\%$ at $x^*/h = 5$.

Table 3 True and estimated friction velocity values from the LES MVG case and five proposed methods, and the error between the estimated and true value at five locations, $x^*/h = 5$, 25, 50, 200, 500

x^*/h	5		25		50		200		500	
Method	U_τ	$E_{U_\tau}(\%)$	U_τ	$E_{U_\tau}(\%)$	U_τ	$E_{U_\tau}(\%)$	U_τ	$E_{U_\tau}(\%)$	U_τ	$E_{U_\tau}(\%)$
Defect	0.0462	0.9	0.0461	3.8	0.0455	4.1	0.0427	0.9	–	–
LLS	0.0562	22.7	0.0396	−10.8	0.0407	−6.9	0.0412	−2.6	0.0405	0.5
MCC	0.0549	19.9	0.0437	−1.6	0.0444	1.6	0.0428	1.2	0.0400	−0.7
inner1	0.0459	0.2	0.0442	−0.4	0.0434	−0.5	0.0421	−0.5	0.0401	−0.5
inner2	0.0460	0.3	0.0442	−0.4	0.0434	−0.5	0.0421	−0.5	0.0401	−0.5
LES MVG	0.0458	-	0.0444	–	0.0437	–	0.0423	–	0.0403	–

MCC is the modified Clauser chart method. LLS is the log-law slope method. The values of LES MVG refer to the true U_τ. U_τ is scaled with U_∞

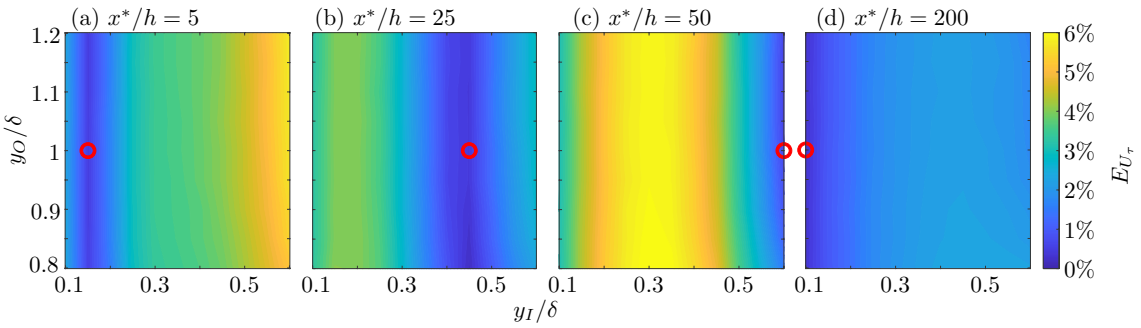

Fig. 4 The mean relative error distribution with varying fitting ranges generated by the defect profile method at $x^*/h = 5$, 25, 50, 200. The fitting ranges vary with two ranges of the inner bound, $0.1 \le y_I/\delta \le 0.6$ and the outer bound, $0.8 \le y_O/\delta \le 1.2$. The red circle refers to the fitting range generating the minimum error

As the log-law methods are based on the existence of the log layer, the inaccurate U_τ determination of the two log-law methods at $x^*/h = 5$ is due to the distorted log-law layer, which can be clearly seen in the velocity deficit in the LES MVG mean velocity profile, as shown in Fig. 3a. Comparison between the two log-law methods shows that the performance of the MCC method is better than the LLS method at $x^*/h = 25$ and 50, where the E_{U_τ} is lower than 2% for the MCC method, but higher than 10% for the LLS method.

The performance of the log-law methods depends on the accurate definition and the thickness of the log-law layer (Walker 2014). The inner and outer bounds of the log-law region are investigated for the two log-law methods. For the LLS method, the fitting range varies with the inner bounds of $0.1 \le y_I^+/\sqrt{\mathrm{Re}_\tau} \le 5$ and the outer bounds of $0.05 \le y_O/\delta \le 0.5$. The inner bound range is selected to cover the true starting of the log-law region, where the upper limit is two times higher than the value suggested for the smooth-wall TBL (Klewicki et al. 2009). The outer bound range is set from the half of the suggested outer bound for the smooth-wall TBL to the outer layer (Marusic et al. 2013). For the MCC method, the log region bounds are defined with the scaling of the displacement thickness δ^*. The location of $y/\delta^* = 0.57$ is the midpoint of the log region for the smooth-wall TBL suggested by Walker (2014). Hence, the inner bound range is selected from the wall of $y_I/\delta^* = 0.01$ –0.57. The outer bound range is chosen from $y_O/\delta^* = 0.58$ –$3\delta^*$ ($\approx 0.5\delta$). Such an outer bound range allows the fitting ranges to extend to the outer layer (Marusic et al. 2013).

The friction velocity error distributions are plotted in Figs. 5 and 6 for the LLS and MCC methods, respectively. Note that the white area is the range with a higher inner bound than the outer bound, which is not applied to the database (i.e., there is no solution). The isoline highlights the error distribution of $E_{U_\tau} <= 3\%$. Figure 5a shows that the LLS method estimates U_τ inaccurately at $x^*/h = 5$, with $E_{U_\tau} > 13\%$. This output is caused by the strong secondary flow induced by the MVGs at the upstream location $x^*/h = 5$ (Chan and Chin 2022). The LLS method starts to be able to determine U_τ with relatively low error, $E_{U_\tau} \le 3\%$ at $x^*/h \ge 25$ (see Fig. 5b–e). The red circle indicates the optimal fitting range for $x^*/h \ge 25$ from $y_I^+/\sqrt{\mathrm{Re}_\tau} = 1.1$ to $y_O/\delta = 0.26$. The isocontour area becomes larger with the downstream development, which indicates that the log-law layer becomes apparent when the MVG TBL flow develops farther downstream.

The MCC method shows a similar performance to the LLS method, which provides an inaccurate U_τ determination with uncertainty of $\ge 12\%$ at $x^*/h = 5$, as shown in Fig. 6a. Figure 6b–e show a similar error distribution for $x^*/h = 25$ –500. These contour maps suggest that the MCC method estimates U_τ inaccurately with a large error of $E_{U_\tau} > 10\%$ when the inner bound $y_I/\delta^* < 0.15$. The outer bound is suggested to be $y_O/\delta^* > 1.2$ to keep the error $E_{U_\tau} < 10\%$. The error reduces with a higher inner bound. However, the low error areas ($E_{U_\tau} = 3\%$) are larger than those of the LLS method. This result indicates that the scaling of the displacement thickness δ^* is more appropriate than the $\sqrt{\mathrm{Re}_\tau}$ and δ in defining the inner and outer bounds of the log-law layer. The universal fitting range indicated by the red circle is from $y_I/\delta^* = 0.27$ to $y_O/\delta^* = 1.445$ for $x^*/h \ge 25$.

4.2.3 Inner-layer method

The two inner-layer methods are found to have an excellent performance with low estimation error, $E_{U_\tau} \le 0.5\%$ at five streamwise locations, as shown in Table 3. The performance is due to the fact that the fitting range includes the near-wall viscous layer measurement of $0.01 \le y^+ \le 70$ from the global mean velocity profiles of the LES MVG database. Therefore, the inner-layer method provides better performance on U_τ determination. To examine the performance of the two inner-layer similarity methods applied to the LES MVG database with the limitations of missing near-wall measurements, various inner bounds of the fitting ranges are investigated. The outer bounds are

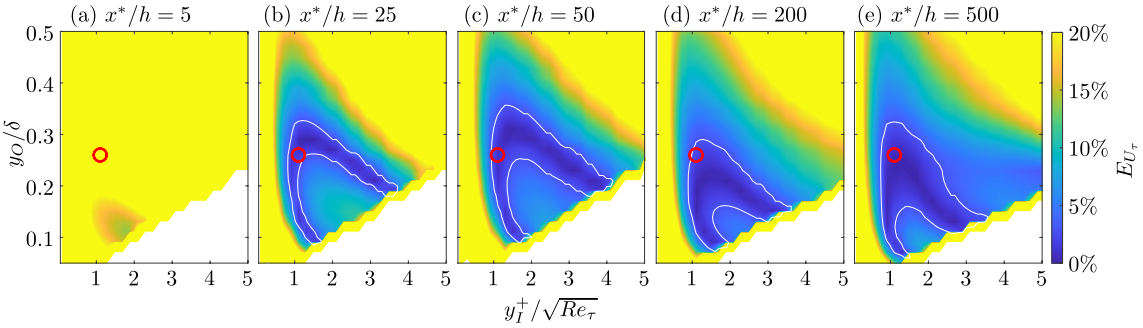

Fig. 5 The mean relative error distribution with varying fitting ranges generated by the LLS method. The fitting ranges vary with two ranges of the inner bound, $0.1 \le y_I^+/\sqrt{\mathrm{Re}_\tau} \le 5$ and the outer bound, $0.05 \le y_O/\delta \le 0.5$. The isoline refers to the error level of 3%. The red circle located within the isoline area ($E_{U_\tau} < 3\%$) indicates the optimum fitting range at $x^*/h = 25$–500

investigated to define the optimal outer bound for different starting points of the fitting range. For the two inner-layer methods, the inner bound range is selected from the wall to $y^+ = 60$, slightly below the buffer layer's top bound at $y^+ = 70$ (Marusic et al. 2010). The conservative outer bound range is chosen as $y_O^+/\sqrt{\mathrm{Re}_\tau} = 1$–20 ($y_O/\delta \approx 0.02$–0.7), where the top limit covers more than half the turbulent boundary layer thicknesses.

The resultant friction velocity is compared with the true LES MVG result, and the U_τ error maps are plotted in Figs. 7 and 8 for the inner1 and inner2 methods, respectively. Here, the inner1 and inner2 methods are based on the Musker function, U^+_{inner}(Musker) (Eq. 6) and the modified Musker function, U^+_{inner}(modified) (Eq. 7). Figure 7(a) shows that the estimation error is less than 3% when using an inner bound $y_I^+ \le 5$ at $x^*/h = 5$. With this inner bound, the U_τ determination is insensitive to the outer bound, even when the outer bound spans over a range, $y_O^+/\sqrt{\mathrm{Re}_\tau} = 1$–20. For downstream locations $x^*/h \ge 25$ (Figs. 7b–e), the low error area ($E_{U_\tau} \le 3\%$) becomes larger than at $x^*/h = 5$, which indicates that the inner1 method estimates U_τ accurately after $x^*/h \ge 25$.

The limitation of the inner1 method is analyzed with the fixed inner bound at $y_I^+ = 20$. The inner1 method inaccurately estimates U_τ with $E_{U_\tau} > 10\%$ when the outer bound exceeds $y_O^+/\sqrt{\mathrm{Re}_\tau} = 10$ ($y_O/\delta \approx 0.46$) at $x^*/h = 25$ (Fig. 7b). Figures 7c–e show that the inner1 method produces $E_{U_\tau} < 10\%$ with outer bounds extending farther away from the wall along the streamwise development, which is up to $y_O^+/\sqrt{\mathrm{Re}_\tau} = 17$ ($y_O/\delta \approx 0.55$) at $x^*/h = 500$. Overall, the inner1 method shows a limited capability to estimate U_τ at $x^*/h = 5$ because the method requires utilizing the mean velocity profile down to $y^+ = 5$ to maintain $E_{U_\tau} < 3\%$. However, the inner1 method shows a good performance in estimating U_τ for $x^*/h \ge 25$, which can use the fitting range of $y_I^+ = 15$ to $y_O^+/\sqrt{\mathrm{Re}_\tau} = 2.5$ to estimate U_τ with $E_{U_\tau} < 3\%$. The U_τ error does not exceed 10%, even with the fitting range from $y_I^+ = 20$ to $y_O/\delta = 0.46$.

The estimation accuracy analysis with various fitting ranges for the inner2 method is plotted in Fig. 8. The low error area ($E_{U_\tau} \le 3\%$) becomes larger for the upstream location at $x^*/h = 5$ but smaller for $x^*/h \ge 25$ compared to the inner1 method. The universal fitting range with a low estimation error $E_{U_\tau} \le 3\%$ can be achieved with an inner bound, $y_I^+ \le 12$ and an outer bound, $y_O^+/\sqrt{\mathrm{Re}_\tau} = 2$. The inner bound of the inner2 method is more likely to be achievable in experiments than that of the inner1 method.

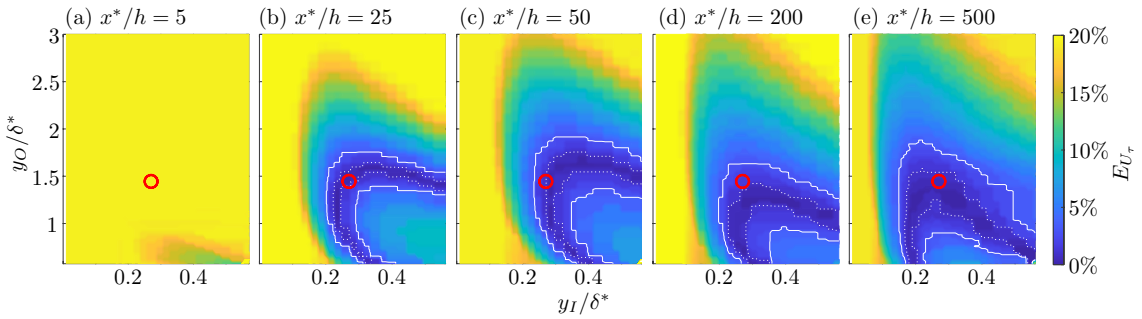

Fig. 6 The mean relative error distribution with varying fitting ranges generated by the MCC method. The fitting ranges vary with two ranges of the inner bound, $0.01 \le y_I/\delta^* \le 0.57$ and the outer bound, $0.58 \le y_O/\delta^* \le 3$. Two isolines refer to the error levels of 3%(solid line) and 1%(dot line). The red circle located within the isoline area ($E_{U_\tau} < 3\%$) indicates the optimum fitting range at $x^*/h = 25$–500

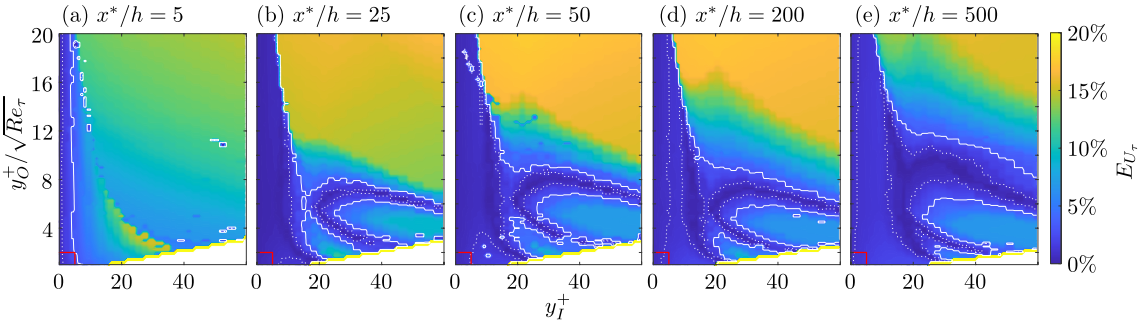

Fig. 7 The mean relative error distribution with varying fitting ranges generated by the inner1 method. The fitting ranges vary with two ranges of the inner bound, $0.03 \le y_I^+ \le 60$ and the outer bound, $1 \le y_O^+/\sqrt{\mathrm{Re}_\tau} \le 20$. Two isolines refer to the error levels of 3%(solid line) and 1%(dot line). The red box located within the isoline area ($E_{U_\tau} \le 3\%$) indicates the optimum fitting ranges at $x^*/h = 5$–500

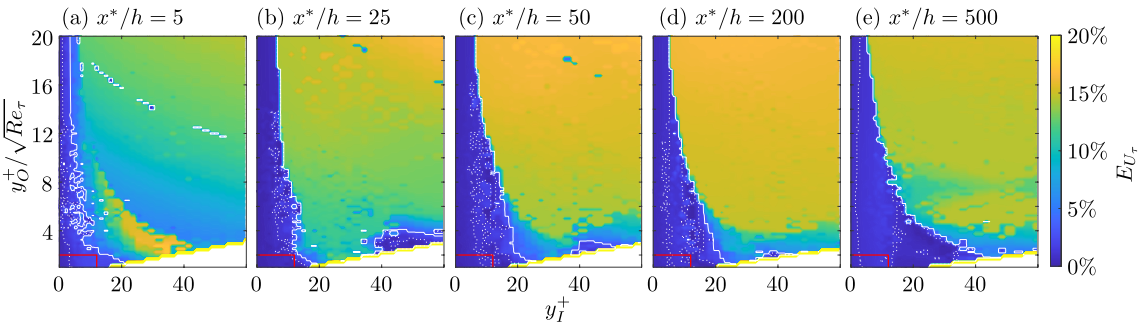

Fig. 8 The mean relative error distribution with varying fitting ranges generated by the inner2 method. The fitting ranges vary with two ranges of the inner bound, $0.03 \le y_I^+ \le 60$ and the outer bound, $1 \le y_O^+/\sqrt{\mathrm{Re}_\tau} \le 20$. Two isolines refer to the error levels of 3%(solid line) and 1%(dot line). The red box located within the isoline area ($E_{U_\tau} \le 3\%$) indicates the optimum fitting ranges at $x^*/h = 5$–500

The contour areas generating a low estimation error of $E_{U_\tau} \le 3\%$ for the two inner-layer methods are plotted in Fig. 9. At $x^*/h = 5$, the contour area of the inner2 method is enlarged for the fitting range with the outer bound, $y_O^+/\sqrt{\mathrm{Re}_\tau} < 8$. The contour area of the inner2 method (red) is smaller than those of the inner1 method (black) for the downstream locations $x^*/h \ge 25$. However, the reduced area is mainly within the fitting range with the inner bound $y_I^+ > 20$ ("C" shape), where the fitting range is not used for both inner-layer similarity methods. This result indicates that the inner2 method can estimate U_τ accurately at the upstream location $x^*/h = 5$ with fixed κ and ϵ.

4.3 Applications of friction velocity determination methods to data-missing LES MVG database

The aim of this study is to assess the performance of the five U_τ-determination methods to determine the suitable method for MVG TBL databases experiencing limitations for the lack of near-wall measurements. Most experimental studies are able to perform smooth-wall TBL measurements with a wall-normal limit of $y^+ \ge 12$ (Kong et al. 2023; Hutchins and Marusic 2007; Samie et al. 2018). According to the hypothesis of the inner-layer similarity methods, the lack of near-wall measurements can significantly affect the U_τ determination performance (as discussed in Sect. 4.2.3), such that it is necessary to investigate the performance of the five U_τ-determination techniques on the LES MVG database with the near-wall data ($y^+ < 12$) removed. Another limitation of the experimental data is that the experiments obtain fewer spanwise individual profiles to determine the pseudo global profile with respect to the LES MVG database (as discussed in Sect. 3.3), e.g., in this study the experimental global profile is obtained by averaging six spanwise individual profiles. Hence, the five U_τ-determination methods are applied to the data-missing LES MVG database, where the limited global velocity profiles are obtained by averaging finite six linear-spaced spanwise profiles within a half spanwise wavelength of one side of MVG, $0 \le z \le \Lambda_z/2$. The limited global velocity profiles also excluded the near-wall data points of $y^+ < 12$. With the true U_τ from the LES MVG database, the uncertainty of the estimated U_τ is computed and analyzed.The LES MVG data is excluded for the near-wall data points $y^+ < 12$. The error between the estimated and true value at five locations, $x^*/h = 5, 25, 50, 200, 500$.

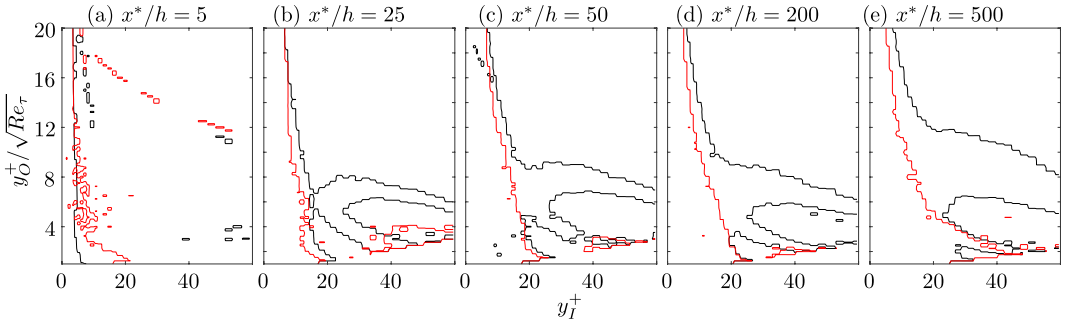

Fig. 9 Comparisons of the error contour of $E_{U_\tau} = 3\%$ between the inner1 (black) and inner2 (red) methods at five streamwise locations $x^*/h = 5$, 25, 50, 200 and 500

The values of LES MVG refer to the true U_τ. U_τ is scaled with U_∞

The application of the five methods to the limited LES MVG database is based on the above-investigated optimized fitting ranges. For the defect profile method, the applied fitting range is $y_I = 0.6\delta$ to $y_O = 1\delta$. The fitting ranges for the MCC and LLS methods are $y_I = 0.27\delta^*$ to $y_O = 1.445\delta^*$ and $y_I^+ = 1.1\sqrt{\mathrm{Re}_\tau}$ to $y_O = 0.26\delta$, which correspond to the red circle in Figs. 6 and 5, respectively. As the data-missing LES MVG profile starts from $y^+ = 12$, the inner bound of the fitting range for the inner1 and inner2 methods is chosen at $y_I^+ = 12$. The outer bound of the fitting range was selected at $y_O^+ = 2\sqrt{\mathrm{Re}_\tau}$, corresponding to the top limit of the universal fitting range indicated by the red box in Fig. 8. This outer bound results in a larger fitting range for higher robustness and also maintains the estimation error of $E_{U_\tau} < 3\%$ for the inner2 method.

The resulting U_τ values and their difference from the true U_τ value are summarized in Table 4. The U_τ values of the defect profile method remain nearly constant along the streamwise development, which does not reflect the influence of the MVGs. Therefore, the defect method is insensitive to the MVGs and cannot determine U_τ accurately by applying a universal fitting range of $y/\delta = 0.6$–1 at $x^*/h \le 50$. However, the defect method provides a rough estimation of U_τ with an uncertainty of $\approx 6\%$ at $x^*/h \ge 5$. Due to the log-law layer distortion, the MCC and LLS methods estimate U_τ inaccurately with $E_{U_\tau} > 16\%$ at $x^*/h = 5$. However, both log-law methods show a good performance in estimating U_τ with $E_{U_\tau} < 3\%$ at $x^*/h \ge 25$, as the log-law region starts to redevelop from $x^*/h = 25$. The inner1 and inner2 methods show better performances than the other methods. The estimation error is less than 5% at $x^*/h = 5$ and less than 2% after $x^*/h = 25$, within the acceptable range (Flack et al. 2007). The inner2 method provides the best overall U_τ determination among the five proposed methods, as this method can achieve $E_{U_\tau} < 3\%$ from the streamwise location $x^*/h \ge 5$.

4.4 Applications of the inner-layer methods with additional floating parameters

To assess the two inner methods with additional two floating parameters ϵ and κ, the inner methods are applied to the data-missing LES MVG database again by relaxing ϵ and κ. Note that ϵ is scaled by δ_0^*. The optimization ranges are $\kappa = 0.3$–0.5 and $\epsilon = -0.01$–0.01. The optimization range of ϵ in the viscous unit is $\epsilon^+ \approx -0.2$–0.2, which can cover the uncertainty range of wall-normal distance experienced by the experimental apparatus (see Sect. 3.5). Three values of $\epsilon = -0.01$, 0 and 0.01 are applied to the LES MVG database to examine the influence of floating ϵ.

Figure 10 shows the contours of the target function value E (see Eq 8) with ranges of constants κ and a at the near-wake station $x^*/h = 5$. Here, the unit of E is $‰$, where

Table 4 Friction velocity values estimated from the five proposed methods with improved fitting range for the data-missing LES MVG database

x^*/h	5		25		50		200		500	
Method	U_τ	$E_{U_\tau}(\%)$	U_τ	$E_{U_\tau}(\%)$	U_τ	$E_{U_\tau}(\%)$	U_τ	$E_{U_\tau}(\%)$	U_τ	$E_{U_\tau}(\%)$
Defect	0.0434	−5.7	0.0431	−2.9	0.0439	0.7	0.0431	1.9	–	–
LLS	0.0594	29.2	0.0439	−0.9	0.0440	0.8	0.0433	2.4	0.0405	0.5
MCC	0.0537	16.9	0.0437	−1.4	0.0446	2.3	0.0430	1.6	0.0403	−0.1
inner1	0.0434	−5.7	0.0446	−0.5	0.0430	−1.4	0.0417	−1.5	0.0395	−2.1
inner2	0.0448	−2.5	0.0452	1.8	0.0434	−0.5	0.0423	0.1	0.0399	−1.2
LES MVG	0.0458	-	0.0444	–	0.0437	–	0.0423	–	0.0403	–

$1‰ = 0.01\%$. The optimal solution is determined by floating κ and shows the lower E for the two inner methods with varied ϵ with a reduction of $E \approx 15‰$, compared with the result of fixed κ. The target function value is also affected by changing ϵ with variation of $E \approx 1.4‰$. The outcome indicates that floating κ and ϵ can find a solution with a lower target function value, compared with the fixed-κ results.

The target function value E and the friction velocity error E_{U_τ} for the applications of the two inner methods with fixed and floating κ at five streamwise stations are summarized in Table 5. The results indicate that the floating-κ cases consistently show lower target function values for all streamwise stations than the fixed-κ results. However, when comparing friction velocity error, it is observed that only the floating-κ cases at $x^*/h = 5$ show lower U_τ error with a maximum reduction of $E_{U_\tau} = 3.4\%$. For $x^*/h = 25$–50, the U_τ error increases with the reduced target function value by floating κ. Introducing variation in ϵ can reduce the target function value for the two inner methods at all streamwise stations. In the cases with different ϵ at each streamwise station, the optimal results with the minimum target function value are highlighted for the two inner methods. However, these highlighted results do not show the lowest friction velocity error. For example, the result of the inner2 method with floating κ at $x^*/h = 5$ shows the lowest target function value of $E = 5.87‰$ with $\epsilon = 0.01$. The friction velocity error is higher than the results of $\epsilon = 0$ and -0.01. Thus, reducing

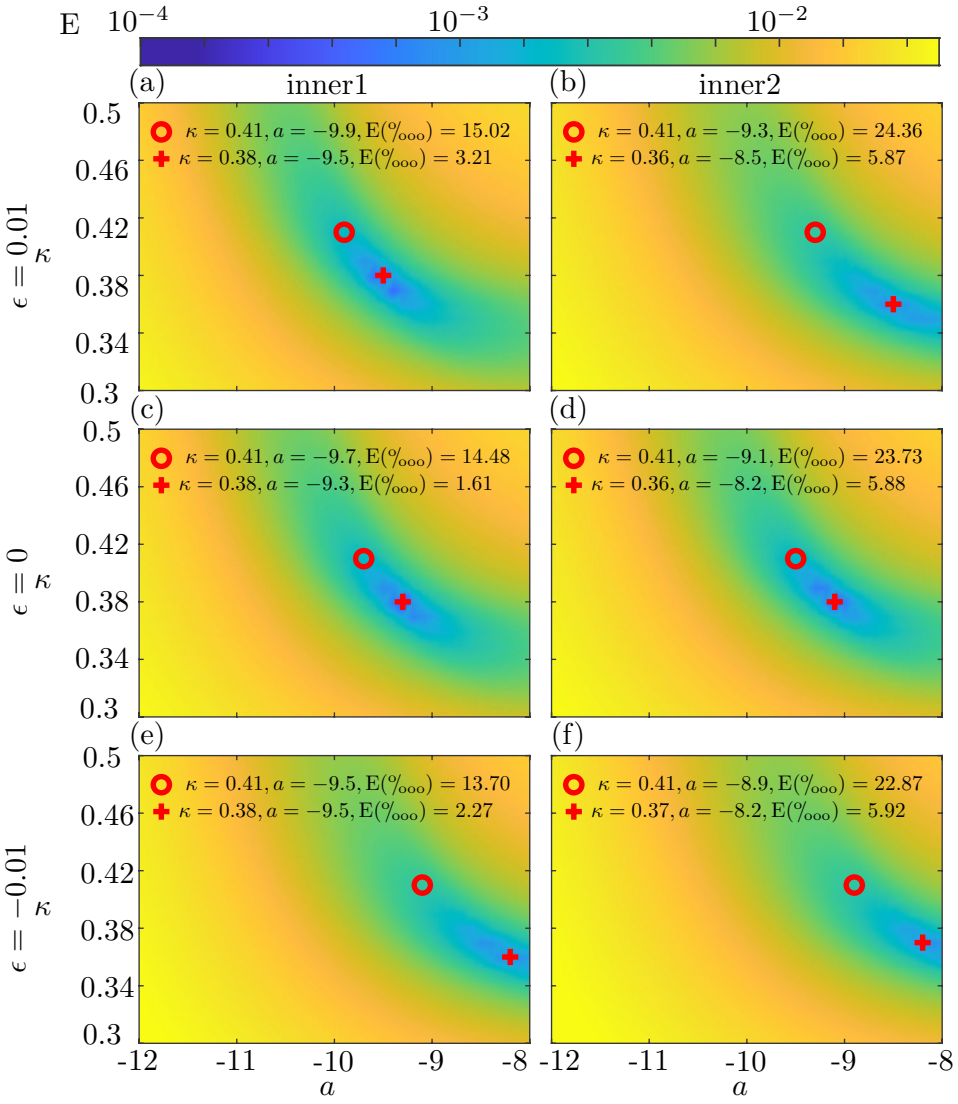

Fig. 10 The error contours of the target function against varying constants a and κ for the applications of the inner1 (a,c,e) and inner2 (b,d,f) methods to the data-missing LES MVG database with three ϵ values at $x^*/h = 5$. The signs + and ∘ indicate the minimum error solutions with floating κ and fixed $\kappa = 0.41$, respectively

the target function value by floating ϵ and κ does not necessarily reduce the friction velocity error for all streamwise locations. Only floating κ for the near-wake case of $x^*/h = 5$ leads to lower U_τ error. Considering that the results of the inner methods with fixed κ and $\epsilon = 0$ show an acceptable error of $|E_{U_\tau}| < 6\%$ at all streamwise stations, the following analysis in Sect. 4.5 utilizes the inner methods with fixed κ and ϵ to experimental MVG TBLs for simplicity.

4.5 Applications of friction velocity determination methods to experimental data

The five U_τ-determination methods are applied to the four experimental datasets of this study with the improved fitting ranges as mentioned in Sect. 4.3. The applications of the inner-layer and log-law methods are conducted with fixed $\kappa = 0.41$ and $\epsilon = 0$ as suggested in Sect. 4.4. All experimental data statistics are based on the spanwise-averaged results of six spanwise profiles. Before analyzing the U_τ determination, the sensitivity of the five U_τ-determination methods to the wall distance error from the present experiment is investigated. Three wall distance shifts of +0.008, 0 and − 0.008 mm are applied to the velocity profiles and the corresponding U_τ values are then estimated from the five U_τ-determination methods. The estimated U_τ is compared with the value estimated from the zero wall distance shifting profiles. For the defect profile, MCC and LLS methods, the U_τ variation is within ±0.7%, which indicates that these three methods are insensitive to the wall distance accuracy of ±0.008 mm. The sensitivity of both inner-layer methods to the wall distance error is similar and larger than that of the other three methods. The averaged variation of U_τ is about 1% for low free-stream speed cases (EXP1 and EXP3) and about ±2.5% for high free-stream speed cases (EXP2 and EXP4). There is one case (EXP2, 5 h), where it is experiencing a high U_τ variation of 5.7%, which may be caused by the inaccurate measurement of the near-wall region. Overall, the influence of the wall distance error for the defect, MCC and LLS methods is negligible and also relatively small for the results from the two inner-layer methods.

The friction drag coefficient is calculated by the estimated friction velocity. The skin friction variation rate, $R = c_f/c_{f,o}$, is plotted against six streamwise locations for the four datasets in Fig. 11, where $c_{f,o}$ is the value of the smooth-wall ZPG TBL calculated by the empirical formula $c_{f,o} = 2\left[1/0.384\ln(Re_\theta) + 4.08\right]^{-2}$ (Osterlund 1999), where Re_θ is the momentum Reynolds number. As a reference, the LES MVG profile shows that the drag coefficient variation reduces monotonously along the downstream development. The difference between the experimental and LES MVG cases of the friction variation rate is quantified as a relative error, $E_R(\%) = 100 \times (R_{\mathrm{EXP}} - R_{\mathrm{ref}})/R_{\mathrm{ref}}$. The mean error for each experimental dataset over the available streamwise locations is defined as, $\epsilon_x|_R(\%) = \langle |E_R| \rangle_x$, where the symbol $\langle \cdot \rangle_x$ and the error ϵ_x denote a streamwise-averaged quantity. Both values are summarized in Table 6.

The defect profile method cannot estimate U_τ accurately for the four experimental datasets as the drag coefficient rates are underestimated with $|E_R| > 10\%$ for $x^*/h \leq 100$, as

Table 5 The target function value and the error of friction velocity from the inner-layer methods with floating/fixed κ and three ϵ values for the data-missing LES MVG database

x^*/h	κ	5		25		50		200		500	
Method		E(‰)	E_{U_τ}(%)	E(‰)	E_{U_τ}(%)	E(‰)	E_{U_τ}(%)	E(‰)	E_{U_τ}(%)	E(‰)	E_{U_τ}(%)
$\epsilon = 0.01$											
inner1	fixed	15.0	−5.8	26.4	−1.9	16.6	−3.1	20.6	−2.7	22.7	−2.7
inner1	floating	3.2	−4.2	**5.3**	−3.3	6.6	−3.5	**6.0**	**−3.3**	**8.0**	**−3.3**
inner2	fixed	24.4	−5.0	15.5	−1.6	4.6	−3.0	3.0	−2.8	1.5	−2.8
inner2	floating	**5.9**	**−1.6**	**1.3**	**−2.9**	3.0	−3.2	3.0	−2.8	**1.5**	**−2.8**
$\epsilon = 0$											
inner1	fixed	14.5	−5.7	30.2	−0.5	16.1	−1.4	19.8	−1.5	21.9	−2.1
inner1	floating	**1.6**	**−2.9**	7.5	−2.2	**6.2**	**−2.5**	7.0	−2.5	10.2	−2.4
inner2	fixed	23.7	−2.5	17.0	1.8	4.7	−0.5	2.3	−1.8	3.6	−1.2
inner2	floating	5.9	−1.2	3.3	−1.7	**1.6**	**−2.1**	**2.3**	**−1.8**	3.6	−1.2
$\epsilon = -0.01$											
inner1	fixed	13.7	−3.6	30.3	0.2	15.5	−1.0	19.9	−0.8	22.7	−0.7
inner1	floating	2.3	−1.9	7.4	−0.9	7.2	−1.8	8.4	−1.6	9.2	−1.4
inner2	fixed	22.9	−2.3	17.0	0.7	5.4	−0.8	3.1	−0.8	3.6	−0.9
inner2	floating	5.9	−0.1	1.9	−0.7	2.8	−1.1	3.1	−0.8	3.6	−0.9

Based on the minimum target function value E, the optimal results for the inner1 and inner2 methods at five streamwise stations are highlighted in bold. The thickness parameters are scaled with δ_0^*

shown in Fig. 11. The underestimated drag coefficient rates, R, are less than one because the region above $y/\delta = 0.6$, showing the outer-layer similarity, is too thin to reflect the actual friction velocity. The two log-law methods (LLS and MCC) show inconsistent behavior from the LES MVG profile for all experimental data. Both methods provide overestimated U_τ at $x^*/h = 5$, and produce an underestimation of U_τ at $x^*/h = 25$ and 50. This outcome may be related to the stronger velocity defect at the three upstream locations ($x^*/h \leq 50$) observed in the experimental velocity profiles (Fig. 3b). The mean estimation error $\epsilon_x|_R$ for the two log-law methods is above 16% (Table 6), which indicates the two log-law are not suitable for U_τ determination of MVG TBL experiments.

In Fig. 11, the results of the inner1 and inner2 methods show a monotonous decrease in the skin friction variation rate along the downstream development. Also, both profiles are similar and collapse to the LES MVG profile for the four experimental datasets. The inner2 method shows better agreement with the LES MVG profile for EXP1 and EXP4 than the inner1 method. For the inner2 method, the mean error, $\epsilon_x|_R$, is 1.6% and 1.4% for EXP1 and EXP4, respectively, while $\epsilon_x|_R = 2.3\%$ and 2.4% for the inner1 method. This indicates that the inner2 method gives a slightly better result for the experimental cases.

The result of the inner2 method is further investigated by analyzing the inner-scaled mean velocity (Fig. 12) and turbulence intensity profiles (Fig. 14), and they are compared with the true-global profiles of the inner-scaled mean velocity and turbulent intensity from the LES MVG database scaled by the true U_τ, as shown in Fig. 13. In Fig. 12, the downward shift of the log-law region reduces with increasing x^*/h for the four sets of MVG TBLs. The downward shift becomes negligible, and the experimental velocity profiles show collapse with each other for streamwise locations $x^*/h \geq 50$. The streamwise development of experimental data is consistent with the LES MVG result, as shown in Fig. 13a.

In Fig. 14a, the inner-layer peaks are located at $y^+ \approx 15$ for all streamwise locations ($x^*/h = 5$–500). The amplitude of peaks increases with increasing x^*/h, and the maximum variation is approximately 28%. In addition, there is a slight hump in the log-law region ($y^+ \approx 74$) at $x^*/h = 5$. This hump becomes clearer and shifts away from the wall with downstream development after $x^*/h = 100$. For the LES MVG result, Fig. 13b also shows that all inner-layer peaks

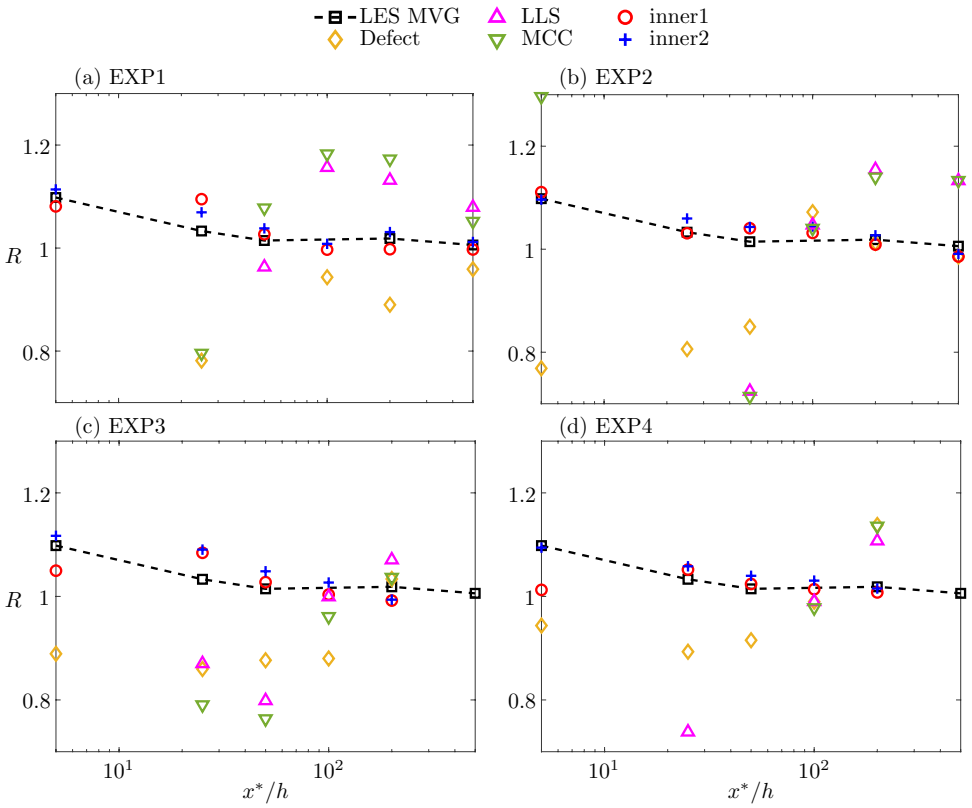

Fig. 11 Skin friction variation rate $R = c_f/c_{f,o}$ against streamwise locations x^*/h for EXP1 (**a**), EXP2 (**b**), EXP3 (**c**) and EXP4 (**d**) by the five proposed methods; Black profile is the LES MVG reference result. Not that some results of LLS and MCC are out of the plotted range and not shown here

Table 6 The skin friction variation rate error $E_R(\%)$ between the estimated results from the experimental datasets by the five proposed techniques and the reference result of the LES MVG database

Method	EXP1							EXP2						
x^*	5 h	25 h	50 h	100 h	200 h	500 h	$\epsilon_x\|_R$	5 h	25 h	50 h	100 h	200 h	500 h	$\epsilon_x\|_R$
Defect	−41.0	−24.4	−31.4	−12.6	**−7.1**	**−4.7**	20.2	−30.0	−22.0	−16.3	**5.5**	**−0.6**	**−2.0**	12.7
LLS	42.1	−41.9	**−5.1**	13.8	11.1	**7.3**	20.2	29.2	−56.9	−28.6	**3.0**	13.4	12.6	24.0
MCC	35.0	−23.0	**6.2**	16.4	15.2	**4.6**	16.7	18.1	−34.4	−29.6	**2.4**	11.9	12.7	18.2
inner1	**−1.6**	**6.0**	**1.2**	**−1.9**	**−2.0**	**−0.9**	**2.3**	**1.2**	**−0.2**	**2.6**	**1.5**	**−1.0**	**−2.0**	**1.4**
inner2	**1.4**	**3.5**	**2.3**	**−0.8**	**1.2**	**0.6**	**1.6**	**−0.2**	**2.6**	**2.8**	**2.8**	**0.8**	**1.5**	**1.8**
	EXP3							EXP4						
Defect	−19.0	−16.8	−13.6	−13.4	**1.5**		12.9	−14.1	−13.5	**−9.8**	**−2.6**	11.7		10.3
LLS	50.4	−15.8	−21.3	**−1.7**	**5.1**		18.9	28.0	−28.6	−31.2	**−2.6**	**8.7**		19.8
MCC	37.1	−23.5	−24.8	**−5.4**	**1.8**		18.5	43.5	−34.3	−34.3	**−3.7**	11.5		25.5
inner1	**−4.4**	**5.0**	**1.3**	**−1.2**	**−2.6**		**2.8**	**−7.8**	**1.8**	**0.9**	**−0.2**	**−1.1**		**2.4**
inner2	**1.7**	**5.6**	**3.3**	**1.1**	**−2.4**		**2.8**	**−0.4**	**2.4**	**2.5**	**1.4**	**−0.3**		**1.4**

$\epsilon_x|_R$ is the streamwise-averaged quantity of the E_R along available streamwise locations for each dataset. Bold values are E_R, $\epsilon_x|_R < \pm 10\%$

are at $y^+ \approx 15$, and the peak amplitude increases by 22% from $x^*/h = 5$–500. The humps of the LES MVG result appear in the log-law region, where their wall-normal locations shift from $y^+ \approx 85$ to 210 for $x^*/h = 5$–50. As the experimental setting of EXP1 is similar to the LES MVG database, the consistent streamwise development of the normalized mean velocity and turbulence intensity profiles indicates the reliability of the estimated friction velocity from the inner2 method.

For different MVG settings, the inner-layer peaks are also located at $y^+ \approx 15$, and the amplitude increases with increasing x^*/h. The humps are also observed for the upstream locations, which appear at $x^*/h \leq 50$ and $x^*/h \leq 100$ for EXP1, EXP3 and EXP2, EXP4, respectively. The humps observed farther downstream in the cases with high free-stream velocity (EXP2, EXP4) indicate that the MVG influence can extend to farther distance with higher free-stream velocity. The investigation of the mechanism of the

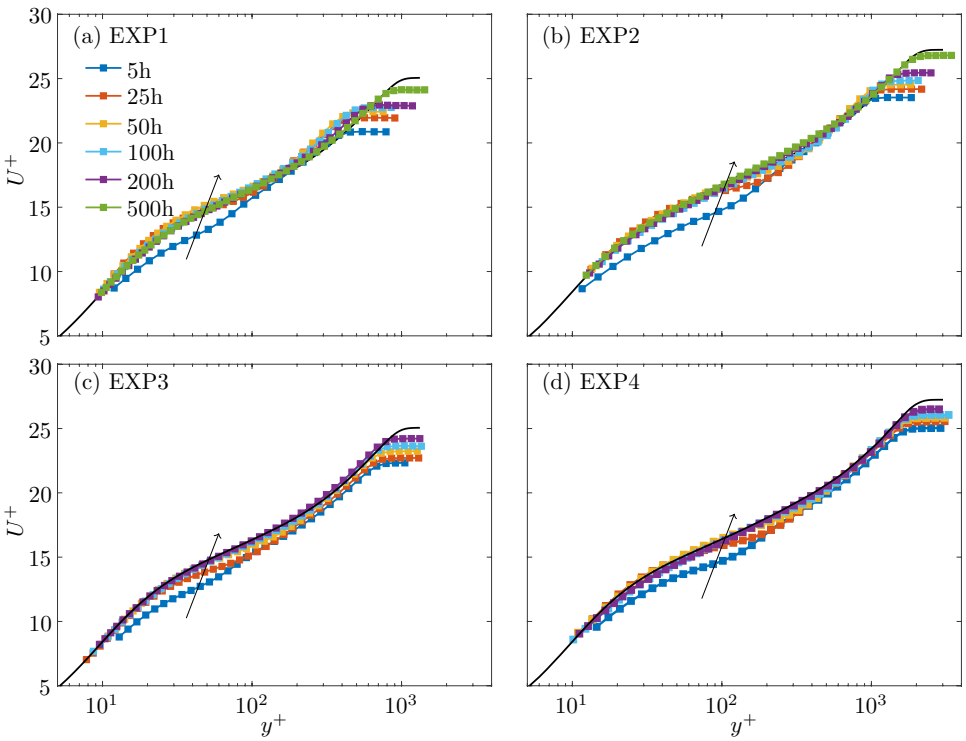

Fig. 12 Inner-scaled mean velocity profiles scaled by the friction velocity of the inner2 method for EXP1 (**a**), EXP2 (**b**), EXP3 (**c**) and EXP4 (**d**); Color code refers to the symbol of × in Table 1. Black solid lines are the smooth-wall TBLs at $\mathrm{Re}_\tau = 900$ (**a**, **c**) and 2000 (**b**, **d**) (Chan et al. 2021). Arrow indicates increasing x^*/h

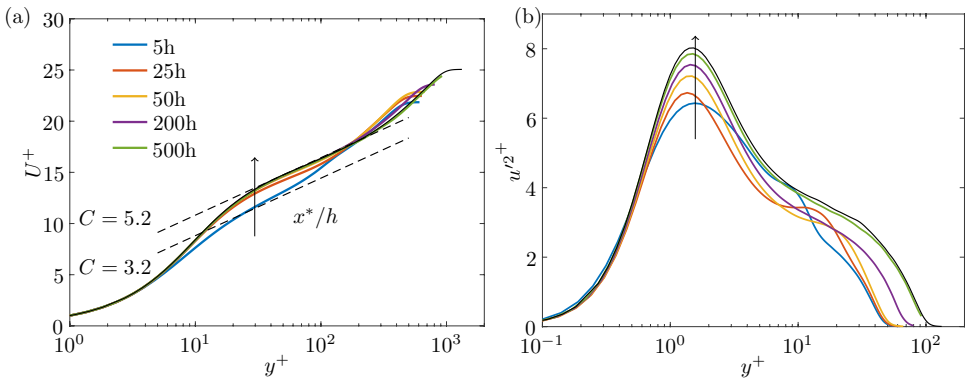

Fig. 13 Inner-scaled mean velocity (**a**) and turbulence intensity (**b**) profiles of LES MVG case by Chan and Chin (2022). Black solid lines are the smooth-wall TBLs at $\mathrm{Re}_\tau = 900$ (Chan et al. 2021). Color code refers to the symbol of × in Table 1

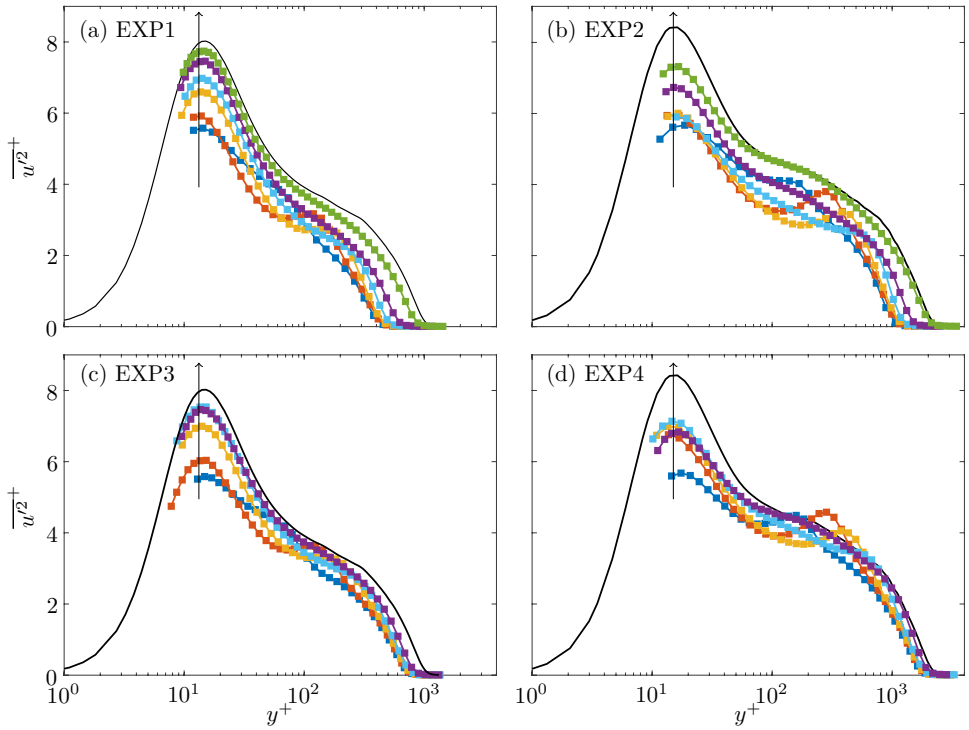

Fig. 14 Inner-scaled turbulence intensity profiles scaled by the friction velocity of the inner2 method for EXP1 (**a**), EXP2 (**b**), EXP3 (**c**) and EXP4 (**d**); Color code refers to the symbol of × in Table 1. Black solid lines are the smooth-wall TBLs at $\mathrm{Re}_\tau = 900$ (a, c) and 2000 (b, d) (Chan et al. 2021). Arrow indicates increasing x^*/h

outer-layer humps is outside the scope of the current study and left as future works. The similar streamwise development of the mean velocity and turbulence intensity between the LES MVG (Fig. 13) and experimental data (Fig. 12 and 14) indicates that the inner2 method is accurate and robust in estimating U_τ for the MVG TBLs.

For the MVG geometry effects, the angle of attack AOA and the MVG height ratio h/δ_0 have been reported as the two most important geometries that affect MVG TBL flow dynamics (Lin 2002; Godard and Stanislas 2006; Shahinfar et al. 2013). A parametric study by Baldacchino et al. (2018) reported similar drag coefficient values for VGs with AOA = 15–20°, considered the optimal range for the application of separation control (Lin 1999; Godard and Stanislas 2006; Lu et al. 2011; Heffron et al. 2018). The similar drag coefficient indicates that the influence of AOA on the inner layer of MVG TBL flows is similar. As the inner2 method relies on the existence of an inner layer, including the viscous, buffer and linear log layers, this assumption is valid for this optimal range of AOA. For MVG TBLs ($0.1 \le h/\delta_0 \le 0.2$), the present study shows that the inner2 method provides accurate U_τ determination for a MVG height ratio range of $h/\delta_0 = 0.1$–0.2, as shown in Figs. 12 and 14. Therefore, the inner2 method is broadly applicable to MVG TBLs with different geometry ratios when the angle of attack is within the optimal range, AOA = 15–20°, and the MVG height ratio is within $h/\delta_0 = 0.1$–0.2. The performance of the inner2 method should be investigated in further works focusing on the effects on a wider range of angle of attack.

Table 7 Summary of applications of the five U_τ -determination techniques to LES MVG and experimental databases

Application		Defect	LLS	MCC	inner1	inner2
LES MVG	$\epsilon_x\|_{U_\tau}(\%)$	2.8	6.8	4.5	2.2	1.2
EXP1–4	$\epsilon_t\|_R(\%)$	14.0	20.7	19.7	2.2	1.9

$\epsilon_x|_{U_\tau}$ is the mean absolute quantity of the E_{U_τ} along the five streamwise locations of the LES MVG database in Table 4. $\epsilon_t|_R$ is the averaged quantity of the $\epsilon_x|_R$ for the four experimental datasets in Table 6

5 Recommendations

Table 7 summarizes the overall performance of the five techniques applied to the LES MVG and experimental data. We define two parameters as measures of the error, which are $\epsilon_x|_{U_\tau}(\%) = \langle|E_{U_\tau}|\rangle_x$ and $\epsilon_t|_R(\%) = \langle\epsilon_x|_R\rangle_t$, where the symbols ϵ_x or $\langle\cdot\rangle_x$ and ϵ_t or $\langle\cdot\rangle_t$ denote the mean quantity along five streamwise locations and over the total four experimental datasets, respectively. The mean error $\epsilon_x|_{U_\tau}$ of the defect profile method is less than 3%, which is within an acceptable range (Flack and Schultz 2014), but the overall mean error ($\epsilon_t|_R$) of the defect method is 14%, which indicates that the defect method does not determine U_τ reliably for experimental MVG TBL profiles. The defect profile method is unable to determine U_τ using the fitting range of $y/\delta = 0.6$–1 at $x^*/h \le 200$ for the LES MVG and experimental databases. This is due to the fitting range for the defect profile method being too short to reflect the actual friction velocity.

For the two log-law methods, $\epsilon_x|_{U_\tau}$ is greater than 3% and $\epsilon_t|_R$ is approximately 20%, which indicates that neither method is suitable for U_τ determination of experimental MVG TBL profiles. Both log-law methods are unreliable in experimental data analysis for upstream locations $x^*/h \le 50$ as the velocity defect extent in the log-law region varies with streamwise locations and MVG settings. Thus, neither method is recommended for the U_τ determination of experimental MVG TBL profiles.

The inner1 and inner2 methods utilize the Musker function and adapt a modified procedure to generate drifted buffer layers as the reference fitting profiles. Both methods show excellent performance in U_τ determination, with lower mean errors than the other three methods for $\epsilon_x|_{U_\tau}$ and $\epsilon_t|_R$. As the inner2 method provides lower overall mean errors in applications of LES MVG and experimental data than that of the inner1 method, the inner2 method is recommended for U_τ determination of MVG TBLs from the near-wake station.

6 Conclusions

This paper investigated various wall-similarity techniques to determine U_τ for MVG TBLs from the near-wake station. The LES MVG database of Chan and Chin (2022) and the new experimental data with four MVG settings were analyzed, and the performance of the five proposed methods was examined, including the defect profile, MCC, LLS, inner1 and inner2 methods. The investigation using the LES MVG database provided the necessary confidence and information on how to perform U_τ determination on wall-bounded flows that are influenced by large-scale vortices (e.g., due to MVGs). The key information is that at least six spanwise velocity profiles over $0 \le z \le \Lambda_z/2$ are needed to obtain an acceptable spanwise-averaged profile.

The "inner" methods utilize the Musker function and adapt a modified procedure by fixing two parameters κ and ϵ and optimizing a free parameter to generate the shifted buffer layers as the reference profiles. The influence of floating κ and ϵ has been investigated by applying the inner methods to the LES MVG database. The outcome reveals that floating κ and ϵ does not necessarily increase the friction velocity estimation accuracy for all streamwise stations. Hence, the inner methods applied to LES and experimental MVG databases in this study are based on the assumption of fixed κ and ϵ. Two inner methods are investigated in the present study, which are the inner1 and inner2 methods. The inner2 method, including the bump function, is recommended. According to the LES MVG database analysis, the inner2 method provides more accurate performance in estimating U_τ as the uncertainty can be maintained at less than 3% from the near-wake station at $x^*/h = 5$, compared with the inner1 method. The mean errors $\epsilon_x|_{U_\tau}$ and $\epsilon_t|_R$ of the inner2 method are acceptable and lower than that of the inner1 method. The inner2 method is also applied to MVG TBLs with different flow conditions at two friction Reynolds numbers and two ratios of h/δ_0. The results of mean velocity and the turbulent intensity profiles suggested that the inner2 method is reasonable and robust for different MVG settings. The inner2 method is suitable for MVG TBLs with the ranges of AOA = 15–20° and $h/\delta_0 = 0.1$–0.2. It is necessary to study other MVG geometries to assess the suitability of the inner2 method. Further work is suggested to implement an independent measurement of shear stress in MVG TBL

experiments to confirm the uncertainty level of the inner2 method.

Acknowledgements The authors thank the Australian Research Council for financial support for this research.

Author contributions J.K obtained all experimental data, wrote the main manuscript text and prepared all figures and tables. C.C provided one of the databases. All authors reviewed the manuscript.

Funding Open Access funding enabled and organized by CAUL and its Member Institutions.

Data availability No datasets were generated or analysed during the current study.

Declarations

Conflict of interest The authors declare they have no conflict of interest.

References

Angele KP, Muhammad-Klingmann B (2005) The effect of streamwise vortices on the turbulence structure of a separating boundary layer. Eur J Mech B/Fluids 24(5):539–554

Baars WJ, Squire DT, Talluru KM et al (2016) Wall-drag measurements of smooth- and rough-wall turbulent boundary layers using a floating element. Exp Fluids 57(5):1–6

Baldacchino D, Ferreira C, Tavernier DD et al (2018) Experimental parameter study for passive vortex generators on a 30% thick airfoil. Wind Energy 21(9):745–765

Buxton OR, Ewenz Rocher M, Rodríguez-López E (2018) Influence of strong perturbations on wall-bounded flows. Phys Rev Fluids 3(1):014605

Chan C, Chin R (2022) Investigation of the influence of miniature vortex generators on the large-scale motions of a turbulent boundary layer. J Fluid Mech 932:A29

Chan CI, Schlatter P, Chin RC (2021) Interscale transport mechanisms in turbulent boundary layers. J Fluid Mech 921:13

Chauhan KA, Nagib HM, Monkewitz PA (2007) On the composite logarithmic profile in zero pressure gradient turbulent boundary layers. In: Collection of technical papers–45th AIAA aerospace sciences meeting, vol 9, pp 6432–6449

Chauhan KA, Monkewitz PA, Nagib HM (2009) Criteria for assessing experiments in zero pressure gradient boundary layers. Fluid Dyn Res 41(2):021404

Chevalier M, Schlatter P, Lundbladh A, et al. (2007) SIMSON : a pseudo-spectral solver for incompressible boundary layer flows. Tech Rep 2007:07, KTH Mechanics, Stockholm, Sweden

Clauser FH (1954) Turbulent boundary layers in adverse pressure gradients. J Aeronaut Sci 21(2):91–108

Coles D (1956) The law of the wake in the turbulent boundary layer. J Fluid Mech 1(2):191–226

Cui G, Pan C, Wu D et al (2019) Effect of drag reducing riblet surface on coherent structure in turbulent boundary layer. Chin J Aeronaut 32(11):2433–2442

Djenidi L, Talluru KM, Antonia RA (2018) Can a turbulent boundary layer become independent of the Reynolds number? J Fluid Mech 851:1–22

Djenidi L, Talluru KM, Antonia RA (2019) A velocity defect chart method for estimating the friction velocity in turbulent boundary layers. Fluid Dyn Res 51(4):045502

Flack KA, Schultz MP (2014) Roughness effects on wall-bounded turbulent flows. Phys Fluids 26(10):101305

Flack KA, Schultz MP, Connelly JS (2007) Examination of a critical roughness height for outer layer similarity. Phys Fluids 19(9):95104

Fransson JH, Talamelli A, Brandt L et al (2006) Delaying transition to turbulence by a passive mechanism. Phys Rev Lett 96(6):1–4

Godard G, Stanislas M (2006) Control of a decelerating boundary layer. Part 1: optimization of passive vortex generators. Aerospace Sci Technol 10(3):181–191

Hakkinen RJ (2004) Reflections on fifty years of skin friction measurement. In: 24th AIAA aerodynamic measurement technology and ground testing conference

Hama F (1954) Boundary-layer characteristics for smooth and rough surfaces. Trans Soc Naval Archit Marine Eng 62:333–358

Heffron AP, Williams JJ, Avital E (2018) Numerical and experimental study of microvortex generators. J Aircr 55(6):2256–2266

Hutchins N, Marusic I (2007) Large-scale influences in near-wall turbulence. Philos Trans Royal Soc A: Math Phys Eng Sci 365(1852):647–664

Hutchins N, Nickels TB, Marusic I et al (2009) Hot-wire spatial resolution issues in wall-bounded turbulence. J Fluid Mech 635:103–136

Kevin K, Monty JP, Bai HL et al (2017) Cross-stream stereoscopic particle image velocimetry of a modified turbulent boundary layer over directional surface pattern. J Fluid Mech 813:412–435

Klewicki J, Fife P, Wei T (2009) On the logarithmic mean profile. J Fluid Mech 638:73–93

Koeltzsch K, Dinkelacker A, Grundmann R (2002) Flow over convergent and divergent wall riblets. Exp Fluids 33(2):346–350

Kong J, Bennetts LG, Nugroho B et al (2023) Systematic study of the Reynolds number and streamwise spacing effects in two-dimensional square-bar rough-wall turbulent boundary layers. Phys Rev Fluids 8(1):014601

Krogstad PÅ, Efros V (2010) Rough wall skin friction measurements using a high resolution surface balance. Int J Heat Fluid Flow 31(3):429–433

Lewthwaite JC, Molland AF, Thomas KW (1984) An investigation into the variation of ship skin frictional resistance with fouling. RINA Trans 127:269–284

Li M, De Silva CM, Rouhi A et al (2019) Recovery of wall-shear stress to equilibrium flow conditions after a rough-to-smooth step change in turbulent boundary layers. J Fluid Mech 872:472–491

Ligrani PM, Bradshaw P (1987) Subminiature hot-wire sensors: development and use. J Phys E: Sci Instrum 20(3):323–332

Lin JC (1999) Control of turbulent boundary-layer separation using micro-vortex generators. 30th Fluid Dynamics Conference

Lin JC (2002) Review of research on low-profile vortex generators to control boundary-layer separation, vol 38. Pergamon

Lin JC, Howard FG, Selby GV (1989) Turbulent flow separation control through passive techniques. AIAA 2nd Shear Flow Conference, 1989

Lin JC, Howard FG, Selby GV (1991) Exploratory study of vortex-generating devices for turbulent flow separation control. In: 29th

Aerospace Sciences Meeting. American Institute of Aeronautics and Astronautics (AIAA)
Lögdberg O, Fransson JH, Alfredsson PH (2009) Streamwise evolution of longitudinal vortices in a turbulent boundary layer. J Fluid Mech 623:27–58
Lu F, Li Q, Shih Y, et al. (2011) Review of Micro Vortex Generators in High-Speed Flow. In: 49th AIAA Aerospace Sciences Meeting including the New Horizons Forum and Aerospace Exposition. American Institute of Aeronautics and Astronautics (AIAA)
Marusic I, McKeon BJ, Monkewitz PA et al (2010) Wall-bounded turbulent flows at high Reynolds numbers: recent advances and key issues. Phys Fluids 22(6):1–24
Marusic I, Monty JP, Hultmark M et al (2013) On the logarithmic region in wall turbulence. J Fluid Mech 716:R3
Monkewitz PA, Chauhan KA, Nagib HM (2007) Self-consistent high-Reynolds-number asymptotics for zero-pressure-gradient turbulent boundary layers. Phys Fluids 19(11):115101
Monty JP, Allen JJ, Lien K et al (2011) Modification of the large-scale features of high Reynolds number wall turbulence by passive surface obtrusions. Exp Fluids 51(6):1755–1763
Musker AJ (1979) Explicit expression for the smooth wall velocity distribution in a turbulent boundary layer. AIAA J 17(6):655–657
Nagib HM, Chauhan KA (2008) Variations of von Kármán coefficient in canonical flows. In: Physics of Fluids, vol 20. American Institute of Physics Inc., p 101518
Nagib HM, Chauhan KA, Monkewitz PA (2007) Approach to an asymptotic state for zero pressure gradient turbulent boundary layers. Philos Trans Royal Soc A: Math Phys Eng Sci 365(1852):755–770
Nocedal J, Wright SJ (2006) Numerical optimization. Springer Series in Operations Research and Financial Engineering pp 1–664
Nugroho B, Hutchins N, Monty JP (2013) Large-scale spanwise periodicity in a turbulent boundary layer induced by highly ordered and directional surface roughness. Int J Heat Fluid Flow 41:90–102
Osterlund JM (1999) Experimental studies of zero pressure-gradient turbulent boundary layer flow. KTH, Stockholm, Sweden
Panaras AG, Lu FK (2015) Micro-vortex generators for shock wave/boundary layer interactions. Prog Aerosp Sci 74:16–47
Perry AE, Li JD (1990) Experimental support for the attached-eddy hypothesis in zero-pressure-gradient turbulent boundary layers. J Fluid Mech 218:405–438
Perry AEAE (1982) Hot-wire anemometry. Clarendon Press
Rodríguez-López E, Bruce PJ, Buxton OR (2015) A robust post-processing method to determine skin friction in turbulent boundary layers from the velocity profile. Exp Fluids 56(4):68
Rodríguez-López E, Bruce PJ, Buxton OR (2016) Near field development of artificially generated high Reynolds number turbulent boundary layers. Phys Rev Fluids 1(7):201–224
Samie M, Marusic I, Hutchins N et al (2018) Fully resolved measurements of turbulent boundary layer flows up to Re_τ=20000. J Fluid Mech 851:391–415
Sattarzadeh SS, Fransson JH, Talamelli A et al (2014) Consecutive turbulence transition delay with reinforced passive control. Phys Rev E–Stat Nonlinear Soft Matter Phys 89(6):061001
Scarano F, Jacob MC, Gojon R et al (2022) Modification of a turbulent boundary layer by circular cavities. Phys Fluids 34(6):65134
Schultz MP, Swain GW (1999) The effect of biofilms on turbulent boundary layers. J Fluids Eng Trans ASME 121(1):44–51
Shahinfar S, Fransson JH, Sattarzadeh SS et al (2013) Scaling of streamwise boundary layer streaks and their ability to reduce skin-friction drag. J Fluid Mech 733:1–32
Shahinfar S, Sattarzadeh SS, Fransson JH (2014) Passive boundary layer control of oblique disturbances by finite-amplitude streaks. J Fluid Mech 749:1–36
Squire DT, Morrill-Winter C, Hutchins N et al (2016) Comparison of turbulent boundary layers over smooth and rough surfaces up to high Reynolds numbers. J Fluid Mech 795:210–240
Talluru KM, Kulandaivelu V, Hutchins N et al (2014) A calibration technique to correct sensor drift issues in hot-wire anemometry. Meas Sci Technol 25(10):105304
Townsend AA (1974) The structure of turbulent shear flow (1976), 2nd edn. Cambridge University Press, Cambridge
Walker JM (2014) The application of wall similarity techniques to determine wall shear velocity in smooth and rough wall turbulent boundary layers. J Fluids Eng Trans ASME 136(5):051204
Xu F, Zhong S, Zhang S (2019) Statistical analysis of vortical structures in turbulent boundary layer over directional grooved surface pattern with spanwise heterogeneity. Phys Fluids 31(8):85110
Ye Q, Schrijer FF, Scarano F (2016) Boundary layer transition mechanisms behind a micro-ramp. J Fluid Mech 793:132–161
Ye Z, Jiang Y, Zhang Y et al (2019) Effects of synthetic jet array on turbulent boundary layer. Int J Heat Technol 37(3):893–898